Master Thesis

Design of large-scale battery pack for regional electric aircraft

Weiming Luo

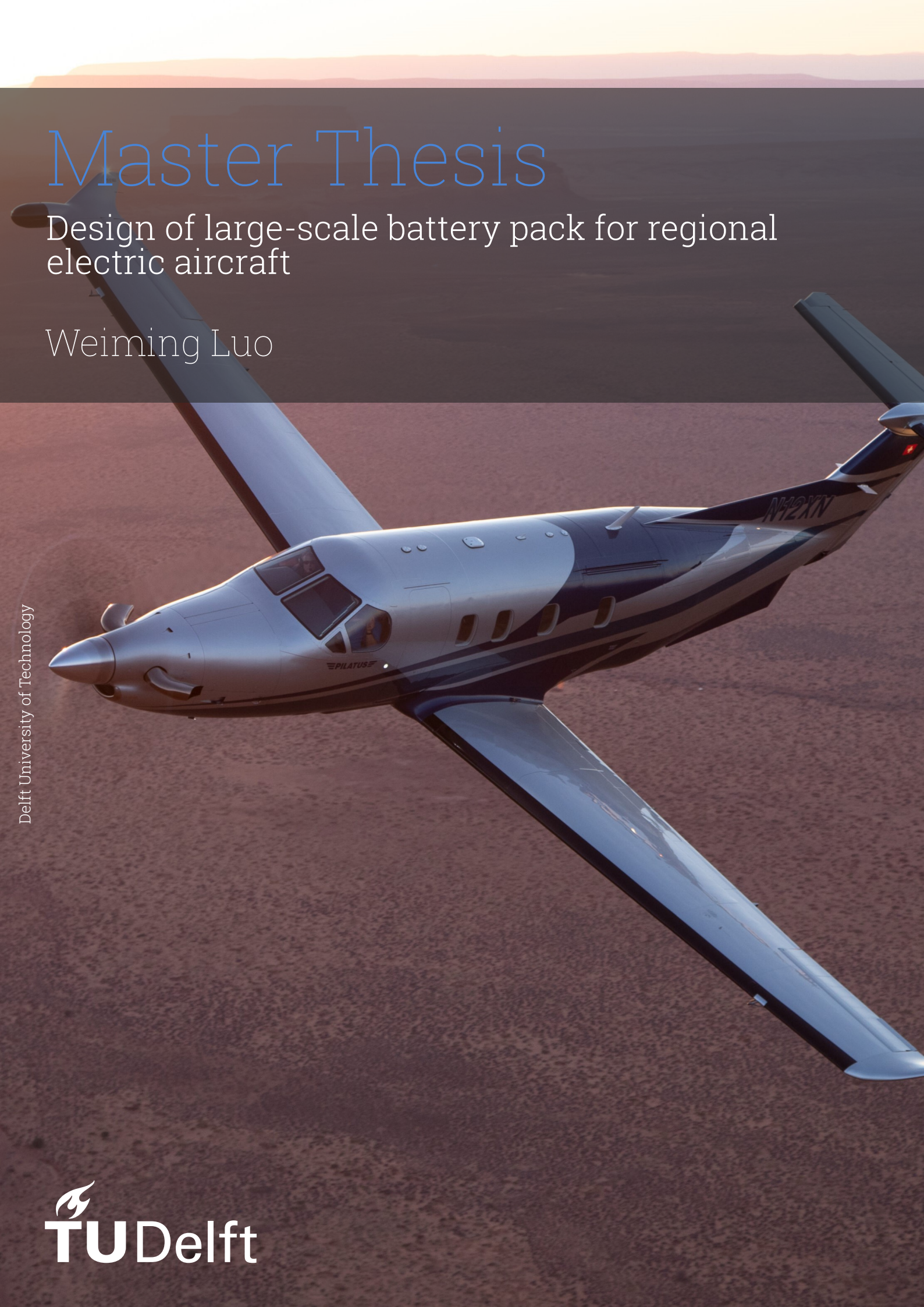

Delft University of Technology

TU Delft

Master Thesis

Design of large-scale battery pack for regional electric aircraft

by

Weiming Luo

Student Name	Student Number
Weiming Luo	5630878

Responsible thesis supervisor: Dr.ir.G.R.Chandra Mouli
Daily co-supervisor: Yawen Liang
Project Duration: January, 2024 - September, 2024
Faculty: Electrical Engineering, Mathematics and Computer Science, TUDelft

TU Delft

Abstract

Since 2007, the impact of aviation industry emissions on climate change has garnered significant scientific attention. Electric aircraft (EA) are emerging as a promising solution to mitigate these effects. However, the design of battery packs capable of withstanding particular obstacles encountered by EA remains a challenge. During flight, critical challenges include meeting flight energy demands with batteries that have a lower energy density compared to conventional fuel aircraft, managing thermal conditions to ensure optimal battery performance, and reducing the weight of the battery system without compromising functionality. The integration of battery thermal management systems (BTMS) to maintain battery efficiency further increases the energy requirements and weight of the battery system. This paper aims to optimize mass energy density and Battery Thermal Management System (BTMS) energy consumption under the condition of meeting the energy, power and temperature requirements of large-scale battery packs for regional All-Electric Aircraft (AEA).

This thesis presents the design of an efficient and lightweight battery pack and its BTMS for pure electric aircraft. Based on a predefined flight cycle, the size of the battery required to meet the energy demands of the electric aircraft is calculated. Using experimental data on battery charging and discharging under varying temperatures and C-rates, an equivalent circuit model (ECM) of the battery cell is established. This ECM predicts the electrical and thermal behavior of the battery during flight. Subsequently, the material selection, specifications, dimensions, and structure of the battery module and BTMS are designed. With a focus on maintaining cell temperature and minimizing BTMS energy consumption, simulations of the packaged battery module are conducted. These simulations are used to explore and optimize various parameters. Finally, the modeling and simulation of the complete battery pack are performed. The simulation results demonstrate that the design effectively meets the operational requirements of pure electric aircraft in the targeted use scenario.

Contents

Abbreviations

AEA All-Electric Aircraft i

APU Auxiliary Power Unit 9

ATAG Air Transport Action Group 1

BMS Battery Management System 45

BTMS Battery Thermal Management System i

CFD Computational fluid dynamics 3

ECM Equivalent Circuit Model 13

ESCD Electric Storage, Conversion, and Distribution 3

EV Electric Vehicle 2

GHG Green House Gas 1

HEA Hybrid Electric Aircraft 2

LIB Lithium-ion Battery 3

MEA More-Electric Aircraft 1

OCV Open Circuit Voltage 16

PCM Phase Change Material 2

PIM Parameter Identification Method 14

SIMPLE Semi-Implicit Method for Pressure-Linked Equations 24

SOC State of Charge 14

SOH State of Health 14

TOGW Take-Off Gross Weight 2

VTOL Vertical Take-off and Landing 3

1 Introduction

1.1. Background and Motivation

Since 2007, the World has been increasingly concerned about the adverse impact on climate change of aviation emissions. In 2022, aviation Green House Gas (GHG) emissions accounted for 3.8% to 4% of total direct emission of Europe, and accounted for 13.9% of transport emission, seconded only to road transport emission[1]. As aviation continues to grow, its emissions problem will become more significant. In 2011, the European Commission set ambitious targets for European aviation by 2050 to protect the environment and the energy supply[2]:

- In 2050 technologies and procedures available allow a 75% reduction in CO2 emissions per passenger kilometre to support the Air Transport Action Group (ATAG) target and a 90% reduction in NOx emissions. The perceived noise emission of flying aircraft is reduced by 65%. These are relative to the capabilities of typical new aircraft in 2000.
- Aircraft movements are emission-free when taxiing.

To meet the demand for aviation emission reduction, technologies such as hybrid/turbine electric, fuel-cell electric, hydrogen electric, bio-fuel electric and AEA are worth further exploration. However, only AEA offer the potential opportunity of long-term zero flight emissions. Meanwhile, AEA can further reduce travel costs than other More-Electric Aircraft (MEA) because fuel is the main air travel expense. In addition, AEA have the potential to reduce aircraft noise[3, 4, 5].

Based on the above driving forces, the number of AEA development projects has expanded rapidly over the past few years[6], with approximately 170 individual projects underway around the world as of February 2020[7]. And alongside the growth of the aircraft electrification market, the demand for aviation-specific battery packs has become increasingly urgent. However, the adaptation of battery packs to the aviation condition has been an under explored domain.

Battery packs in AEA face much greater power supply challenges than those in conventional aircraft. As for conventional aircraft, the engine power is converted into four main types of energy: pneumatic, mechanical, hydraulic, and electrical energy[8]. The thrust to move the aircraft is generated by the engine. In addition to the thrust power requirement, the most important power consumers in a conventional aircraft are: avionics systems (electrical), pumps (mechanical or hydraulic), drive systems (hydraulic), environmental control systems (pneumatic), and wing anti-icing systems (pneumatic). In AEA, the energy for most of the systems including thrust will be provided by batteries. Given that the energy density of the battery is much lower than that of conventional aviation fuel, the size of the battery pack in AEA will be large. The impact of the strengths and weaknesses of the battery pack design is also amplified. The importance of battery pack design has therefore increased.

1.2. Current Research Status

This section discusses existing literature related to the field of battery packs for AEA as well as BTMS design.

Current approaches to aircraft sizing in the literature are almost logically consistent, with differences mainly in the terms used and the sequence of processes.

Mattingly's method[9] is a representative method used in several researches[10, 11, 12]. Its process consists of three main parts: constraint analysis, mission analysis, and weight estimation. Constraint analysis ensure to meet the thrust-weight ratio and wing load constraints. By mission analysis, estimated fuel or battery weight (measured by Take-Off Gross Weight (TOGW)) was calculated from flight performance equations. Weight estimation combines thrust-weight ratio and wing load information to finally determine the three quantities of thrust, wing area and weight. Liang et al. [10] determined the aircraft size based on data from reference conventional aircraft. They also found that compared with the reference fuel aircraft, the range of the converted AEA is greatly reduced due to the energy density limitation. The all-electric modification of the Cessna 172R reduces the range by about 80%. With the increase of the payload of the retrofit AEA, the energy density demand of the battery pack also increases accordingly. This means that in order to have sufficient range, the mass energy density of the AEA battery pack design is important. The mass energy density loss from cell to pack needs to be minimized, so excellent battery pack structure design is required.

Some designs of aircraft battery pack geometry have been done in the existing literature.

Chin et al. [13] presented a method for determining the optimal package shape for a range of material choices. Existing solid battery packs with filling of aluminum and Phase Change Material (PCM) were examined. And the structure of the variant battery pack with grid layout and honeycomb layout with hole added is optimized. The optimization targeted at minimum weight with different mass energy density and geometry. Optimization geometric variables include cell spacing and internal notch size. It was found that the PCM interstitial materials with high latent heat and low thermal conductivity were heavier than aluminum in their respective optimal structures. In addition, it is found that the staggered hexagonal layout is more mass efficient when the cell energy density is low, while the grid layout is better when the cell energy density is high.
Heit and Liscouet-Hanke [14] estimated the efficiency rate of weight energy density and volume energy density with various shape cells in the cell-to-module and module-to-pack processes. The accurate of estimation is verified by actual AEA battery pack parameters, with errors below ±10% for the cylindrical cell and ±2% compared to the Pipistrel aircraft.

Numerous designs of BTMS have been done in the existing literature. The application scenarios include Electric Vehicle (EV),Hybrid Electric Aircraft (HEA),MEA and AEA.

Xia, Cao, and Bi [15] discussed series, series-parallel, and parallel cooling configurations for air and liquid cooled battery modules in EV application. It is concluded that liquid cooling, especially direct liquid cooling has high potential. In addition, three main thermal processes are divided: heat generation, heat transfer and heat dissipation. For large-size batteries, multi-scale multi-dimensional coupling models have been developed. It has been recognized that enhancing thermal boundary conditions helps to reduce the average cell temperature but enlarge the temperature gradient in the cell. The gradient is related to local irreversible heating, thermal resistance, current distribution and other factors.

Kim et al. [16] numerically explore the use of PCM in BTMS for a typical one-hour flight in the 3D domain. The PCM of 298.15K and 308.15K melting temperatures tested in this thesis can prevent the battery temperature from exceeding the thermal limit. This study found that the PCM thermal conductivity has a negligible effect on the performance of PCM, which increases exponentially with the latent heat of melting of PCM. However, as a passive temperature control, PCM of PCM lacks the ability to adjust to different requirements during flight phases.

Kellermann et al. [17] designed and optimized the BTMS for a 19-seat HEA, considering the case when the ambient temperature is higher than the operating temperature of the battery cell due to hot weather. A numerical model of a thermoelectric cooling heat pump combined with a fan-driven air heat

exchanger is developed and the parameters associated with its performance are determined. The best optimization results resulted in only a 2% increase in aircraft take-off weight.

Kuijpers, Kampen, and Hofman [18] designed a 304 kWh battery system with BTMS for light electric passenger aircraft, ensuring fault redundancy through two parallel switching battery packs. The optimization results highlight the better performance of cold plate water cooling over air cooling. The addition of 9.9 kW water cooling BTMS resulted in an increase in weight of 16.5% (387 kg), reducing the simulated range of the aircraft from 480 km to 410 km..

Annapragada et al. [19] has conducted design studies for battery thermal harvesting for the aerospace industry to reduce weight and parasitic power. It is found that even at high efficiency, the Electric Storage, Conversion, and Distribution (ESCD) systems of hybrid electric aircraft exhaust a significant amount of heat at relatively low temperatures. Three evaluation metrics are proposed for BTMS: the ratio of the heat exchanger mass to the battery mass, the temperature difference between the center of the cell and the fluid, and the pressure drop required to achieve cooling. It is also found that using liquids rather than air as coolants can reduced pressure drop.

Fredericks et al. [20] calculated and analyzed the performance index of the next generation battery to achieve Vertical Take-off and Landing (VTOL) aircraft. In this thesis, the power requirements of electric VTOL are studied, and a 650V, 52.5 kWh Lithium-ion Battery (LIB) pack using advanced technology is constructed. The estimation results in a discharge rate of 4C for take-off and close to 5C for landing. The ratio of heat generation to battery pack size due to a high discharge C-rate is found to be more than one order of magnitude higher than the equivalent range of an EV and more than two orders of magnitude higher than that of an electric semi-truck. The predicted discharge C-rate of turboprop aircraft is also relatively high. Therefore, different from the traditional strategies used in EVs, the application of these two AEA requires unique thermal management solutions. The design of BTMS needs to ensure acceptable battery performance and eliminate the risk of thermal runaway propagation to the entire battery pack.

Other research devoted to assessing the parameters and performance of AEA battery pack designs. Sripad, Bills, and Viswanathan [21] reviewed the current understanding of battery-related safety issues in the context of urban and regional electric aviation and conducts a discussion of battery capacity attenuation and power attenuation. Barke et al. [22] evaluated the environmental, economic, and social impacts of eight potential battery systems for short-range aircraft from a life-cycle perspective. They completed some of the late work of the design under their set design scheme.

1.3. Research Gap

With comprehensive reference to previous work in the field of **EA!** (**EA!**) battery pack structure and BTMS system design, a large number of works are aimed at HEA and other aircraft with relatively small battery pack weight ratio, and lack of thermal performance analysis of the battery pack throughout the flight. Therefore, the focus of this thesis is:

- Most of the previous research focuses on the cooling effect of BTMS. Due to the possible heating and cooling requirements of the battery pack during the flight, this thesis applied the control of the BTMS and explore the thermal performance when switching between heating and cooling states. And some control optimizations are done for BTMS flow rate control.
- Existing studies mostly used the steady-state assumption and are not able to capture the transient heat transfer process between different components, which may lead to inaccurate performance evaluation. In this thesis, Computational fluid dynamics (CFD) method is used to perform transient simulation of the whole flight process to observe the time-dependent performance of BTMS.
- Because of the complexity of the model, the previous study lacks simulation of the entirety of large battery pack in the aircraft. In this thesis, the thermal performance of a multi-module battery

pack is initially simulated based on simplification assumptions.

1.4. Research Goal

In this thesis, the goal of the battery pack design is to minimize the mass and volume of battery pack while meeting the power and energy requirements of the AEA and maintaining a stable and uniform battery temperature throughout the flight.

Specifically, the battery pack design and optimization are mainly divided into two parts: geometric design and BTMS design. The geometry is optimized to achieve the highest possible mass and volumetric energy density. The design objectives of BTMS control are to achieve thermal stability, thermal uniformity, and regulation speed.

1.5. Research Questions

The following questions dominate the research direction presented in this thesis: *1) How to analyse the AEA flight energy demand and how will this decide the size of battery pack?*
2) How to simulate the battery cell electrical and thermal behavior in the discharge?
3) How to design the BTMS of the battery module?
4) Is the design of the battery pack appropriate?

2

Flight Analysis and Battery Pack Sizing

To design the battery pack, its total energy specification should be determined first. In this chapter, firstly the typical flight process of the AEA model is analysed in Section.2.1 to obtain the energy requirement of AEA. Then the battery cell type selection is made among existing battery cell chemical types in Section.2.2 to select the appropriate cell type for the battery pack. Finally, the number of cells in the battery pack is sized in Section.2.3.

2.1. Flight Mission Analysis

In this thesis, the aircraft under consideration has a capacity of less than 20 passengers. In order to meet the traffic between the major airports in Europe, the cruising range target is set to 220km. With this range, commuting between small regional or remote utility airports can also be achieved.

To determine the design requirements of the battery pack, the first step is to determine the specifications of the AEA. In view of the limited actual experimental data of AEA, to make the design easier to transform from theoretical data to practical outcome, this thesis modifies the existing mature commercial aircraft specification to meet the flight parameter requirements of AEA. In this way, the aerodynamics and part of the flight mechanics of the conventional aircraft, which has already been verified in test flights, can be extended to the AEA. The PC-12 model was selected as the reference model and some of its specifications are shown in Table.2.1. The relevant parameters of the retrofit PC-12 have already been estimate[10] and shown in Table.2.2.

Aircraft Model	Reference Conventional Aircraft PC-12
Take-Off gross Mass $W_{\text{tot,ref}}$	4740kg
Engine power $P_{\text{peak,ref}}$	890kW
Wing Area $A_{\text{w,ref}}$	25.8m^2
Wing Span $b_{\text{w,ref}}$	16.28m
Lift to Drag Ratio $L_{\text{D,ref}}$	16.07
Power loading $\frac{P_{\text{peak,ref}}}{W_{\text{tot}}}$	0.0522N/W
Wing loading $\frac{W_{\text{tot,ref}}}{A_{\text{w,ref}}}$	1801.6N/m^2

Table 2.1: Technical specifications of the reference aircraft PC-12

Table 2.2: Technical specifications of conventional reference aircraft(PC12) and Designed AEA

Aircraft Model	Designed electric aircraft
Take-off mass W_{tot}/g	10059.2kg
Propeller Revolution Speed n	1700rpm
Propeller Diameter D	105inch
Wing Area A_{w}	49.8m^2
Difference between cruise altitude and airport altitude Δh	4575.4m
Power loading $\frac{P_{\text{peak}}}{W_{\text{tot}}}$	0.0522N/W
Wing loading $\frac{W_{\text{tot}}}{A_{\text{w}}}$	1981.5N/m^2
Static Thrust Coefficient	0.73
Zero-lift Drag Coefficient $c_{0\text{D}}$	0.025
Induced Drag Correction Factor k	0.0303
Take-off Lift Coefficient $c_{\text{l,to}}$	1.7
Take-off Friction Coefficient μ	0.03
Climb Gradient α_{cl}	0.083
Descent Gradient α_{cl}	-0.083

Based on the typical missions of the existing aircraft, it was decided to consider five main phases in the flight mission: take-off, climb, cruise, descent and landing. Because the landing phase is with minimal energy consumption and lowest power requirements[23], while the time is relatively short, this phase is ignored in this thesis.

Table 2.3: U.S. Standard Atmosphere Air Density and Altitude Profile[24]

Altitude above Sea Level [m]	**Air Density [kg/m^3]**
0	1.225
1000	1.112
2000	1.007
3000	0.9093
4000	0.8194
5000	0.7364

Table 2.4: Air Density of Main Phases

Phase	**Air Density [kg/m^3]**
Take-off $\rho_{\text{a,to}}$	1.225kg/m^3
Climb $\rho_{\text{a,cl}}$	0.9983kg/m^3
Cruise $\rho_{\text{a,cr}}$	0.7716kg/m^3
Descent $\rho_{\text{a,de}}$	0.9983kg/m^3

The U.S. standard atmosphere air density profile below 5000m above sea level is shown in Table,2.3. With linear correlation coefficient of 0.9984, air density is considered to be linear in altitude within the scope of the flight, so the air density during climb and descent phase is calculated by interpolation and shown in Table.2.4:

$$\rho_{\text{a,cl}} = \rho_{\text{a,de}} = (\rho_{\text{a,to}} + \rho_{\text{a,cr}})/2 \tag{2.1}$$

1) Take-off Phase: The aircraft faces the greatest power demand during take-off. Assuming the same power-loading ratio (All the variables appearing in this thesis use SI units):

$$\frac{P_{\text{peak}}}{W_{\text{tot}}} = \frac{P_{\text{peak,ref}}}{W_{\text{tot,ref}}} \tag{2.2}$$

where $P_{\text{peak,ref}}$ and P_{peak} are respectively the peak power of reference conventional aircraft and retrofit AEA during the take-off process.

The aircraft is considered to have zero velocity in the direction perpendicular to the runway. The characteristics of the take-off phase can be described by the balance of forces in the direction of horizontal acceleration of the aircraft:

$$\frac{dv}{d\text{t}} = \frac{F_{\text{t}} - F_{\text{d}} - F_{\text{f}}}{W_{\text{tot}}/g} \tag{2.3}$$

where v and t are the aircraft velocity and time, $\frac{dv}{d\text{t}}$ is the acceleration of aircraft, F_{t}, F_{d} F_{f} are respectively the thrust force, the aerodynamic drag and the friction, g is the gravitational acceleration. During

take-off phase the velocity and the acceleration are horizontal.
During take-off, the efficiency of the propeller varies, as calculated:

$$\begin{aligned} \eta_{\text{prop}} &= \frac{2}{1+\sqrt{1+c_t}} \\ c_t &= \frac{2F_t}{\eta_{\text{prop}}\rho_{a,to}v^2\pi {r_{\text{prop}}}^2} \end{aligned} \tag{2.4}$$

Then the thrust force is expressed as follows:

$$F_t = \frac{P_{em,to}}{\eta_{\text{prop}}\eta_{em}\eta_{gb}v_h} \tag{2.5}$$

where $P_{em,to}$ is the electric motor power during take-off, η_{prop}, η_{em}, η_{gb} are respectively the efficiency of the propeller, the electric motor and the gearbox, shown in Table.2.5.

Component	**Efficiency**
Propeller	80% (during cruising)
Electric motor	95%
Gearbox	99%
DC/DC converter	99.5%
DC/AC inverter (controller)	99.5%
Cabling	98.5%
Battery pack	96%

Table 2.5: Efficiency of electric propulsion system components with state-of-the-art technology in AEA

The aerodynamic drag is expressed as follows:

$$F_d = \frac{1}{2}\rho_{a,to}v^2A_w\left(c_{0D} + k{c_{l,to}}^2\right) \tag{2.6}$$

where ρ_a is the air density at airport altitude, A_w is the wing area of the aircraft, c_{0D} is the zero-lift drag coefficient, $c_{l,to}$ is the lift coefficient during take-off, k is the induced drag correction factor. Note that these coefficients vary according to the angle of attack in every phase.

The friction is expressed as follows:

$$F_f = \mu\left(W_{tot} - \frac{1}{2}\rho_{a,to}v^2A_wc_l\right) \tag{2.7}$$

where μ is the friction coefficient of tire-ground interaction. When the aircraft takes off, the tires are not rotated by the power unit. Its role is to support the weight of the aircraft and provide rolling while taxiing on the ground, so the sign of the μ is positive.

At the start of the take-off phase, the static thrust is estimated[25]:

$$F_{t,st} = 1.283\times10^{-12}n^2D^4\rho_{a,to}K_tg \tag{2.8}$$

where $F_{t,st}$ is the static thrust provided by propeller, n is the propeller revolution speed (Revolution Per Minute), D is the diameter of the propeller in inches, K_t is the static thrust coefficient.

At the end of the take-off phase, in the vertical direction lift is equal to TOGW:

$$W_{tot} = \frac{1}{2}\rho_{a,to}{v_{to,e}}^2A_wc_{to} \tag{2.9}$$

where $v_{to,e}$ is the take-off equilibrium speed.

Because the use of active control keeps the propeller operating close to its maximum efficiency point for each flight condition[26], it is assumed that the motor power remains relatively constant and always maximum during the take-off phase. In this thesis, Eq.2.3 to 2.7 is iteratively calculated by the single-step method with one second iteration time interval. At iteration start, static trust is calculated by Eq.2.8. When v_{h} is not less than the take-off equilibrium speed, the iteration ends, and the time used in the take-off phase is obtained.

Therefore, the battery energy consumption during take-off can be estimated as follows:

$$E_{\mathrm{to}} = \frac{P_{\mathrm{em,to}}}{\eta_{\mathrm{E}}} t_{\mathrm{to}} \tag{2.10}$$

$$\eta_{\mathrm{E}} = \eta_{\mathrm{DC/DC}} \cdot \eta_{\mathrm{DC/AC}} \cdot \eta_{\mathrm{cab}} \cdot \eta_{\mathrm{bat}} \tag{2.11}$$

where E_{to} is the total battery energy consumption during take-off, t_{to} is the take-off time, η_{E} is the total efficiency of the electric propulsion system, which is the product of converter efficiency $\eta_{\mathrm{DC/DC}}$, inverter efficiency $\eta_{\mathrm{DC/AC}}$, cable efficiency η_{bat} and battery efficiency η_{bat}.

2) Climb and Descent Phase: It is assumed that the acceleration of the aircraft during the climbing and descending phases is negligible[26]. Thus:

$$v = \sqrt{1+\alpha^2} v_{\mathrm{to,e}} \tag{2.12}$$

$$v_{\mathrm{v}} = \alpha v_{\mathrm{to,e}} \tag{2.13}$$

where v_{v} is the vertical velocity of the aircraft. Similar to Eq.2.9, based on the balance of forces at lift direction acting on the aircraft:

$$W_{\mathrm{tot}} \frac{1}{\sqrt{1+\alpha^2}} \approx W_{\mathrm{tot}} = \frac{1}{2} \rho_{\mathrm{a}} v^2 A_{\mathrm{w}} c_{\mathrm{l}} \tag{2.14}$$

Based on the balance of forces at trust direction acting on the aircraft:

$$\begin{aligned} F_{\mathrm{t}} &= W_{\mathrm{tot}} \frac{\alpha}{\sqrt{1+\alpha^2}} + F_{\mathrm{d}} \\ &= W_{\mathrm{tot}} \frac{\alpha}{\sqrt{1+\alpha^2}} + \frac{1}{2} \rho_{\mathrm{a}} v^2 A_{\mathrm{w}} \left(c_0 + k {c_{\mathrm{l}}}^2 \right) \end{aligned} \tag{2.15}$$

Then, expressions for the climb and descent powers can be obtained as:

$$\begin{aligned} P &= F_{\mathrm{t}} v \\ &= W_{\mathrm{tot}} v_{\mathrm{v}} + \frac{1}{2} \rho_{\mathrm{a}} v^3 A_{\mathrm{w}} \left(c_0 + k {c_{\mathrm{l}}}^2 \right) \\ &= W_{\mathrm{tot}} v_{\mathrm{v}} + \frac{1}{2} \rho_{\mathrm{a}} v^3 A_{\mathrm{w}} c_0 + \frac{2k {W_{\mathrm{tot}}}^2}{\rho_{\mathrm{a}} v A_{\mathrm{w}}} \end{aligned} \tag{2.16}$$

where ρ_{a} is the air density during climb and descent phase.

Similar to Eq.2.10, the battery energy consumption in the climbing and descending phases can be calculated. The duration of the climb and descent phases can be calculated from the vertical distance difference between take-off, landing and cruising altitude. In this thesis, it is assumed that the take-off and landing airports are at the same altitude, so the vertical distance of climb and descent are the same.

$$E_{\mathrm{cl}} = \frac{P_{\mathrm{cl}}}{\eta_{\mathrm{E}} \eta_{\mathrm{prop}} \eta_{\mathrm{em}} \eta_{\mathrm{gb}}} \cdot \frac{\Delta h}{v_{\mathrm{v}}} \tag{2.17}$$

$$E_{\mathrm{de}} = \frac{P_{\mathrm{de}}}{\eta_{\mathrm{E}} \eta_{\mathrm{prop}} \eta_{\mathrm{em}} \eta_{\mathrm{gb}}} \cdot \frac{\Delta h}{v_{\mathrm{v}}} \tag{2.18}$$

where Δh is the difference between cruise altitude and airport altitude.

3) Cruising and Reserve Phase: Similar to Eq.2.16, the cruise power is expressed as:

$$P_{\mathrm{cr}} = \frac{1}{2}\rho_{\mathrm{cr}} v^3 A_{\mathrm{w}} c_0 + \frac{2kW_{\mathrm{tot}}{}^2}{\cdot \rho_{\mathrm{cr}} v A_{\mathrm{w}}} \tag{2.19}$$

The time of the cruise phase is derived from the required range. Therefore, the energy consumption of the cruise phase is as follows:

$$E_{\mathrm{cr}} = \frac{P_{\mathrm{cr}}}{\eta_{\mathrm{E}}\eta_{\mathrm{prop}}\eta_{\mathrm{em}}\eta_{\mathrm{gb}}} \cdot \frac{R}{v} \tag{2.20}$$

where R is the range of the aircraft design requirement.

To reduce security risks, considering reserve enough energy to support an additional 15 minutes of cruising, then the reserve energy is expressed as follows:

$$E_{\mathrm{res}} = \frac{P_{\mathrm{cr}} t_{\mathrm{res}}}{\eta_{\mathrm{E}}\eta_{\mathrm{prop}}\eta_{\mathrm{em}}\eta_{\mathrm{gb}}} \tag{2.21}$$

where t_{res} is the reserve time.

The above calculation yields the battery energy required for the propulsion system throughout the flight. In addition, the Auxiliary Power Unit (APU) also needs battery function. Typically, the energy consumption of the APU accounts for 2% of the total energy consumption during a typical flight[27]. Therefore, the required battery pack energy can be calculated as follows:

$$\begin{aligned} E_{\mathrm{dem}} &= E_{\mathrm{to}} + E_{\mathrm{cl}} + E_{\mathrm{cr}} + E_{\mathrm{de}} + E_{\mathrm{res}} + E_{\mathrm{APU}} \\ &= (E_{\mathrm{to}} + E_{\mathrm{cl}} + E_{\mathrm{cr}} + E_{\mathrm{de}} + E_{\mathrm{res}}) \cdot 102\% \end{aligned} \tag{2.22}$$

where E_{dem} is energy demand of battery pack, E_{APU} is the energy consumption of the APU.

By calculation, the power and energy profile of the designed AEA is shown in Table.2.6 and Fig.2.1.

Table 2.6: Technical specifications of conventional reference aircraft(PC12) and Designed AEA

Phase	Power [kW]	Energy Requirement [kWh]
Take-off	1888.75	9.4438
Climb	1040.06	300.7554
Cruise	408.563	471.5117
Descent	34.2109	9.8928
Total		807.4359

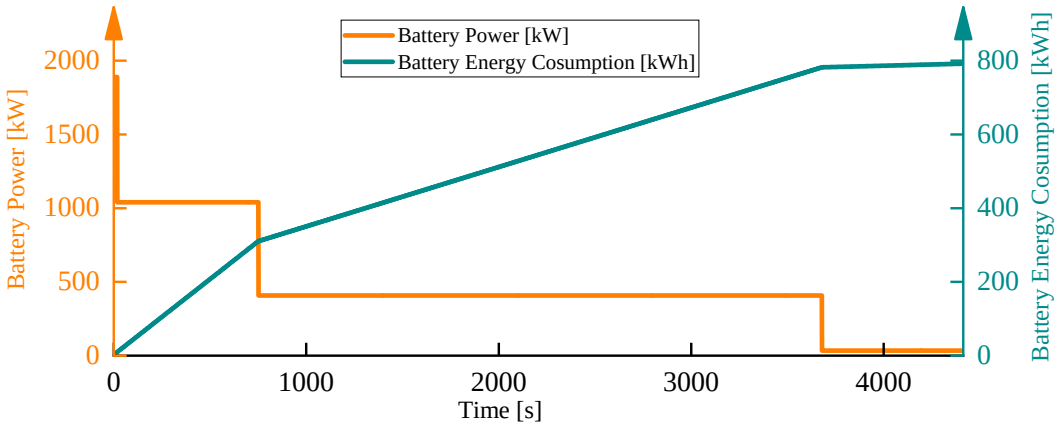

Figure 2.1: Power profile of designed AEA during a typical regional flight

Fig.2.2 depicts the altitude and temperature of four typical operation phases of the flights considered in this thesis. The model of the relationship between atmospheric temperature and altitude is as follows[28]:

$$T_a = T_s - 0.00649h \tag{2.23}$$

Where T_a is the atmospheric temperature, T_s is the earth surface temperature, h is the altitude.

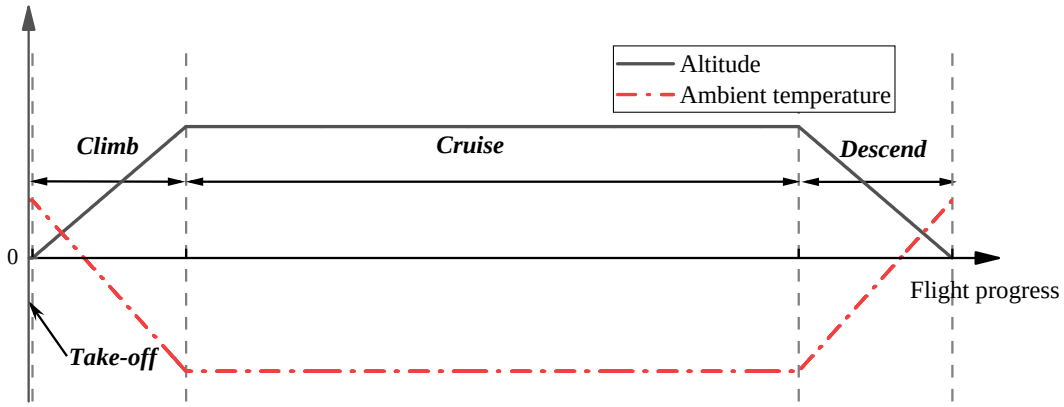

Figure 2.2: Simplified profiles of height and ambient temperature during a typical regional flight

2.2. Battery Cell Selection

After obtaining the target load of the battery pack, the type of battery cell needs to be selected. As the only power supply for AEA, batteries face various performance requirements in energy density, power density, life time, safety. The existing battery cell types are difficult to achieve high energy density, high charge and discharge cycle and low cost at the same time. In Table 2.7, comparison of some critical parameters across different chemical types of battery is given to select the best battery cell type for the mission.

Table 2.7: Comparison of different chemical types of battery[29][30][31][32]

Battery cell type	Abbreviation	Nominal Voltage [V]	Mass specific energy [Wh/kg]	Cycle	Price
Lead acid	Pb-acid	2.0	35	1000	Low
Nickel cadmium	Ni-Cd	1.2	50-80	2000	Low
Nickel-metal hydride	Ni-MH	1.2	75	<3000	Low
Lithium cobalt oxide	LCO	3.7-3.9	150	500-1000	Medium
Lithium nickel, manganese cobalt oxide	NMC	3.6-4.0	170-240	1000-2000	Medium
Lithium iron phosphate	LFP	3.3	90-160	1000-2000	High
Lithium-sulfur	Li-S	2.5	350-650	300	Low
Lithium-air	Li-air	2.9	1300-2000 (theoretical)	100	High

For the energy demand of AEA, mass specific energy, volume specific energy, mass power density, temperature influence and cycle life are used as the prior selection criteria in this thesis. Batteries with

high mass specific energy and volume specific energy have low weight and small volume with the same energy storage requirements, which is beneficial to save aircraft load and space. Meanwhile, batteries for AEA should be able to operate efficiently over a wide temperature range(-10 to 60°C), thereby reducing the burden and energy consumption of BTMS. And in order to reduce maintenance costs and safety risks, the cycle life of batteries should be as large as possible. For comprehensive evaluation in the above aspects, due to its high energy density, well-established technology, and strong battery supply chain which is ready to use, NMC batteries (a popular type of LIB) is selected in this thesis.

NMC batteries are traditionally available in three shapes: cylindrical, prismatic, and pouch (soft cladding). Cylindrical batteries offer superior mechanical stability. The circular structure ensures that internal pressure from side reactions is evenly distributed along the circumference[33][34]. However, at the battery module and pack levels, cylindrical batteries have lower space utilization compared to prismatic and pouch batteries due to the gaps created by their circular cross-sections. But thermal management is also easier. Thermal and mechanical safety issues are significant for aircraft design, so cylindrical batteries are selected in this thesis.

The characteristic properties of simulated battery model in this thesis is shown in Table 2.8.

Table 2.8: The characteristic properties of simulated battery model Samsung INR18650-35E[32]

	NMC battery
Manufacturer	Samsung
Model	INR18650-35E
Dimension	Height: Maximum 65.25mm Diameter: Maximum Φ 18.55mm
Nominal discharge capacity C_n	Min 3350mAh
Charging voltage V_{ch}	4.2V
Nominal voltage V_n	3.60V
Charging method	CC-CV
Standard charging current $I_{ch,st}$	1700mA
Maximum charging current $I_{ch,max}$	2000mA
Maximum discharging current $I_{d,max}$	13000mA
Discharge Cut-off voltage V_{min}	2.65V
Cell Weight M_{cell}	50g
Operating temperature	Charge: 0 to 45°C Discharge: -10 to 60°C

2.3. Battery Pack Sizing

The power supply profile of the battery pack during flight is indispensable for its sizing. The battery pack should:

- Satisfy the existing highest power output: Power requirements are typically orders of magnitude greater during take-off than at other processes[35]. Take-off power will serve as a reference threshold for battery pack sizing.
- Meet the total energy demand of whole range with enough margin. The target range has been set at 220 km to meet the minimum flight distance requirement between most of Europe's major airports. And for safety reasons, the battery pack will reserve energy equivalent to 15 minutes of cruising time to hovering behavior or possible accidents.

According to the cruising and reserve calculation in this chapter, if the battery size just meets 100% discharge in the case of emergency landing, 87.35% energy will be consumed at the end of the normal flight with rest of the energy reserved.

In the powertrain, the DC output of battery packs is connected to the DC/DC converter. There-

fore,

$$V_{\text{pack}} = V_{\text{n}} n_{\text{s}} \geq V_{\text{DC/DC,in}} \tag{2.24}$$

where V_{pack} is the voltage of battery pack, n_{s} is the series connection number of battery cell in the pack, $V_{\text{DC/DC,in}}$ is the input voltage of DC/DC converter. In order to reduce the current and thus the diameter of the harness, a HVDC grid of 3kV(±1.5kV) is proposed[36]. A conservative value of 1.5kV is used in this thesis.

The size of the battery has to meet the total energy demand of the flight. Therefore,

$$E_{\text{pack}} = V_{\text{pack}} C_{\text{n}} n_{\text{p}} \geq E_{\text{dem}} \tag{2.25}$$

where E_{pack} is the total energy of battery pack, n_{p} is the parallel connection number of battery cell in the pack.

Based on the calculations in this chapter, the parameters of the designed battery pack are given in Table 2.9.

Table 2.9: The specifications of designed battery pack

	NMC battery pack
Size E_{pack}	809.672kWh
Voltage	1500V
Cell number n_{tot}	67137
Cell series number n_{s}	417
Cell parallel number n_{y}	161
Maximum discharge power $P_{\text{d,max}}$	1934kW (for continuous discharge) 3142kW (not for contimuous discharge)

3

Electric and Thermal Model of battery cell

To understand the electrical and thermal behavior of the cell, it is necessary to construct its model. The electric model of battery cell is introduced, verified by experimental data and analysed in Section.3.1. The thermal model of cell is simplified in Section.3.2.

3.1. Electric Model of Lithum-ion Battery Cell

In this thesis, the Thevenin Equivalent Circuit Model (ECM) was adapted to model the dynamic discharging and thermal behavior of a cell. Compared with other battery models, ECM can better simulate the battery characteristics without increasing the complexity[37].

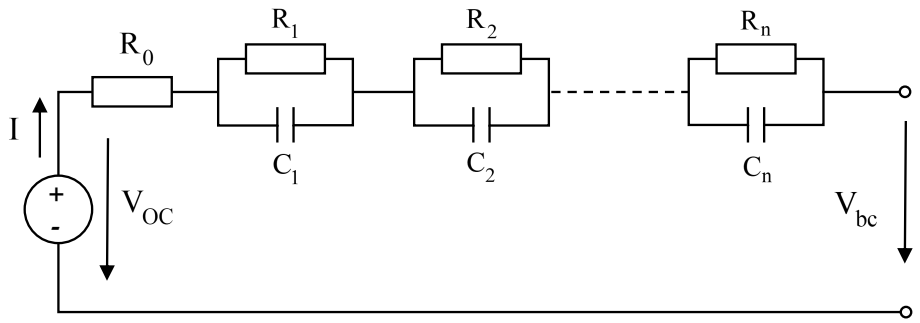

Figure 3.1: Typical n-order Thevenin ECM of a battery cell

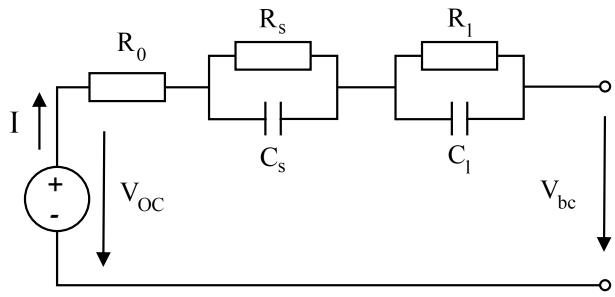

Figure 3.2: 2-order Thevenin ECM of a battery cell

In this thesis, the second-order Thevenin ECM as shown in Fig.3.2, is applied. The model consists of V_{OC}, R_0 and multiple RC combinations. V_{OC} and V_{bc} respectively are the open circuit voltage and terminal

voltage of the battery cell. R_0 is the ohmic resistance, which includes the surface layer resistance and the volume resistance of the battery cell. R_l and R_s are polarization resistances. C_l and C_s are polarization capacitors. Each of the two RC combination has a time constant. The time constant τ_s of R_s and C_s is in the range of several seconds, showing the short-term characteristics of the battery.

$$\tau_s = R_s C_s \tag{3.1}$$

The time constant τ_l of R_l and C_l is in the range of tens of seconds or longer, showing the long-term characteristics of the concentration polarization of the cell.

$$\tau_l = R_l C_l \tag{3.2}$$

The mathmatical expression of ECM is as below:

$$V_{bc} = V_{OC} - IR_0 - V_s - V_l \tag{3.3}$$

$$I = \frac{V_s}{R_s} + C_s \frac{dV_s}{dt} \tag{3.4}$$

$$I = \frac{V_l}{R_l} + C_l \frac{dV_l}{dt} \tag{3.5}$$

or,

$$V_s(t) = V_s(0)\, e^{\frac{-t}{\tau_s}} + IR_s \left(1 - e^{\frac{-t}{\tau_s}}\right) \tag{3.6}$$

$$V_l(t) = V_l(0)\, e^{\frac{-t}{\tau_l}} + IR_l \left(1 - e^{\frac{-t}{\tau_l}}\right) \tag{3.7}$$

where t is the time, I is the current through the circuit, positive for discharge and negative for charge.

3.1.1. Model Parameter Identification Method

The accuracy of the model parameters largely depends on the Parameter Identification Method (PIM). PIMs can be divided into static methods and dynamic methods. Static PIM is to use fixed parameter values to measure circuit components, and its disadvantage is to ignore that the work of the battery is a dynamic process. The parameter values will depend on State of Charge (SOC), discharge rate, temperature and State of Health (SOH) in this ECM. Therefore, dynamic identification is used to imitate the circuit component performance. In fact, during battery cycling aging, the evaluation of SOH must continue until the end of the life of the battery cell. And, the test must be repeated on a large number of cells to obtain reliable results. Thus, the impact of SOH is neglected in this thesis due to the complexity and test time considerations.

3.1.2. Parameter Extraction Experiment

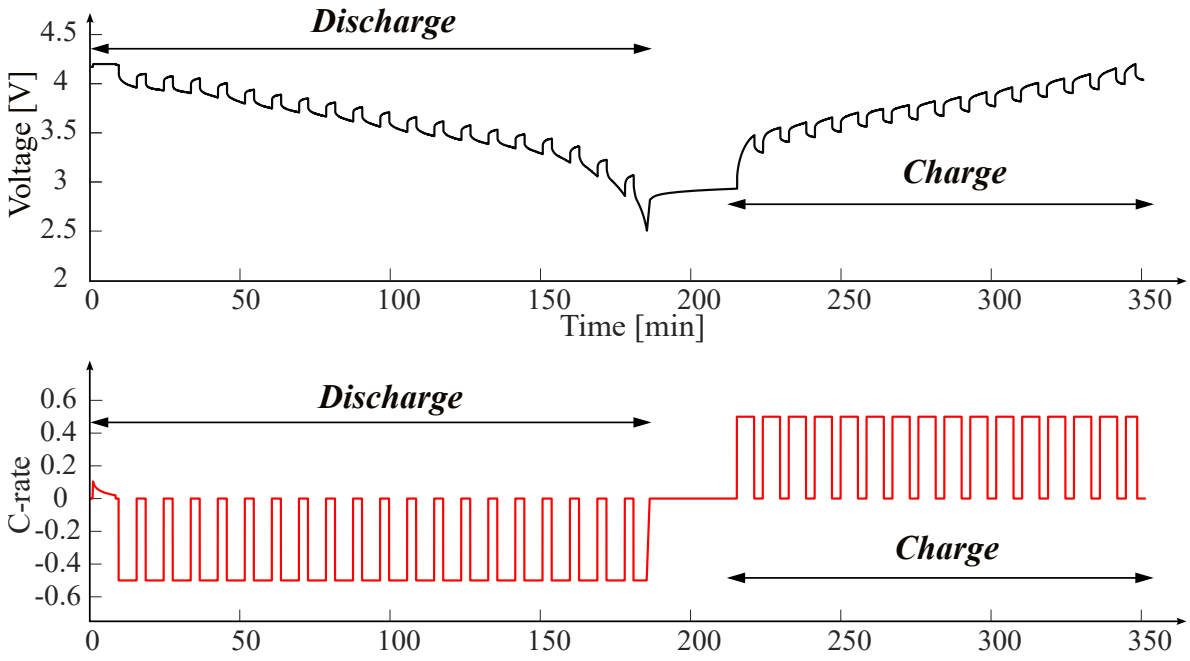

Figure 3.3: Voltage and current within the test cycle

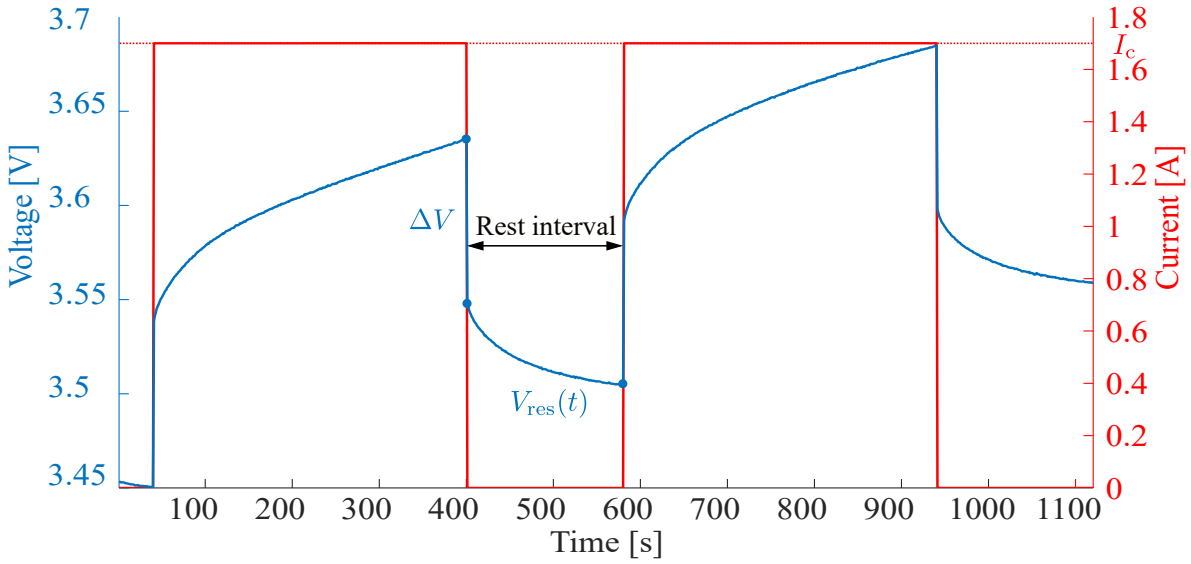

Figure 3.4: Zommed Voltage and current within the test cycle

The experiment tests the parameters in two parts:

Internal Resistance and Capacitance Test
Following the existing ECM battery parameter test method[38][39], the current of the pulse test cycle in this experiment is shown in Fig.3.3. Three battery cells were used for each test set to reduce chance errors. The constant current and constant voltage (CC-CV) charging procedure was consistent before each set of tests to ensure the same initial SOC of battery cells. The same test procedure was repeated under the following conditions:

- When the ambient temperature was maintained at 25°C, the C-rate is set as: 0.1C, 0.2C, 0.3C, 0.4C, 0.5C, 0.6C, 0.7C, 0.8C, 0.9C, 1C, 1.5C, 2C. 12 cases in total
- When the C-rate was maintained at 0.5C, the ambient temperature is set as: 0°C, 10°C, 20°C, 30°C, 40°C. 5 cases in total

Open Circuit Voltage Test
Considering the hysteresis effect of the Open Circuit Voltage (OCV), the residence time of the test OCV was extended from 3 minutes to 180 minutes under the same experimental procedure as the test of the internal resistance and capacitance. The experiment was repeated at different temperatures to explore the effect of temperature on OCV.

Test Data Post-processing
SOC indicates the amount of charges stored in the battery cell as a percentage of its rated charge capacity. This value can not be determined directly, so Coulomb counting is applied to derive this value in this thesis:

$$SOC\,(t) = SOC\,(0) - 100\frac{\int_0^t Idt}{\mathrm{C_n}} \tag{3.8}$$

After the same charging procedure before test, SOC_0 is considered to be 100. To ensure that the SOC is as stable as possible when collecting a set of other data, a period that the current is close to zero is selected. Hence the sampling is preformed during the relaxation time between charging(or discharging) pulses as shown in Fig.3.4. At the end of the current pulse, the battery switches from the loaded state to the relaxed state. The instantaneous voltage drop (rise) is used to determine the internal ohmic resistance:

$$R_0 = \frac{\Delta V}{I_\mathrm{c}} \tag{3.9}$$

where ΔV is the instantaneous voltage change, positive for discharge and negative for charge; I_c is the injected current during pulse, positive for discharge and negative for charge.

After switching to the relaxed state, the battery still takes some time to reach equilibrium, which is due to the limited response rate of the chemical reactions inside the battery cell to current changes. In ECM, this process is embodied in short- and long-duration transient RC combinations.

$$V_{res}\,(t) = V_\mathrm{s}\,(t) + V_\mathrm{l}\,(t) \tag{3.10}$$

where $V_\mathrm{res}(t)$ is the remaining voltage. Thus, to obtain parameters of two RC combinations, the remaining voltage curve during rest time were fitted with the nonlinear least squares method using equations (3.1), (3.2), (3.6), (3.7) and (3.10).

3.1.3. Model Parameter Identification Result

After obtaining the test profile that incorporates discharge pulses that take place at different state of SOC, temperature and C-rate, functions are used to reflect the performance of the battery under various conditions. As shown in Fig.3.5, the open circuit voltage of the battery cell does not change significantly with respect to temperature, so the open circuit voltage of the battery cell is considered as a monotonic function of SOC. For all other parameters, it is found that it is affected by SOC, temperature, and C-rate. After attempts of curve fitting, a sufficient parameter identification equation is obtained as shown in Eq.3.11 to 3.16.

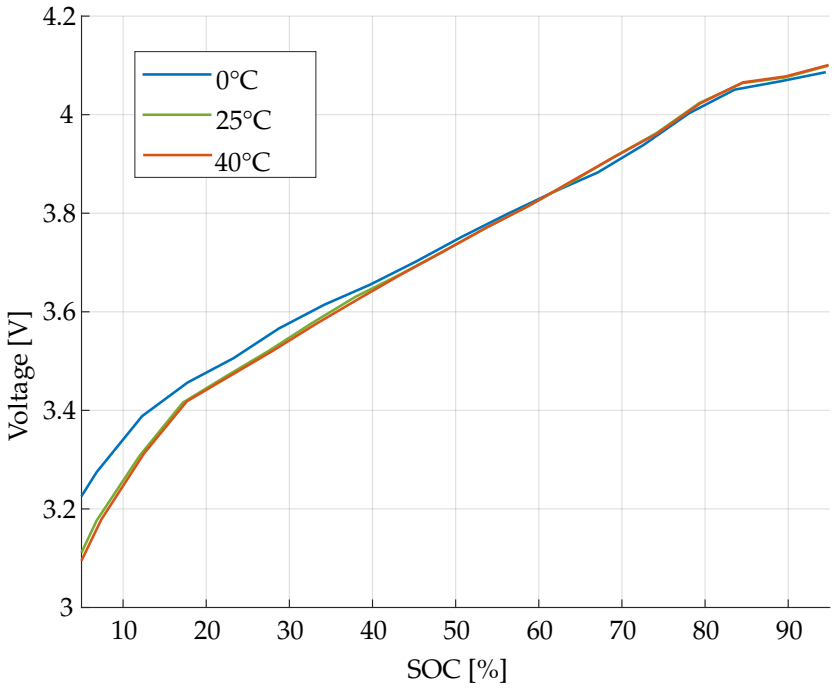

Figure 3.5: Test result of open circuit voltage at discharging rate of 0.5C with different temperature

$$V_{OC}(SOC) = a_{1OCV}e^{-a_{2OCV}SOC} + a_{3OCV} + a_{4OCV}SOC \tag{3.11}$$

$$\begin{aligned} R_0(SOC, T_c, C_{rate}) =& (a_{1R0} + a_{2R0}SOC + a_{3R0}SOC^2 + a_{4R0}SOC^3 + a_{5R0}SOC^4) \cdot b_{1R0}e^{\left(\frac{b_{2R0}}{T_c - b_{3R0}}\right)} \\ & \cdot (c_{1R0}{C_{rate}}^{c_{2R0}} + c_{3R0}) \end{aligned} \tag{3.12}$$

$$\begin{aligned} R_s(SOC, T_c, C_{rate}) =& (a_{1Rs} + a_{2Rs}SOC + a_{3Rs}SOC^2 + a_{4Rs}SOC^3 + a_{5Rs}SOC^4 + a_{6Rs}SOC^5 + a_{7Rs}SOC^6) \\ & \cdot (b_{1Rs} + b_{2Rs}T_c + b_{3Rs}T_c^2 + b_{4Rs}T_c^3 + b_{5Rs}T_c^4 + b_{6Rs}T_c^5) \\ & \cdot (c_{1Rs} + c_{2Rs}C_{rate} + c_{3Rs}{C_{rate}}^2 + c_{4Rs}{C_{rate}}^3 + c_{5Rs}{C_{rate}}^4) \end{aligned} \tag{3.13}$$

$$\begin{aligned} C_s(SOC, T_c, C_{rate}) =& (a_{1Cs} + a_{2Cs}SOC + a_{3Cs}SOC^2 + a_{4Cs}SOC^3 + a_{5Cs}SOC^4 + a_{6Cs}SOC^5 + a_{7Cs}SOC^6) \\ & \cdot (b_{1Rs} + b_{2Rs}T_c + b_{3Rs}T_c^2 + b_{4Rs}T_c^3 + b_{5Rs}T_c^4 + b_{6Rs}T_c^5) \cdot (c_{1Cs}{C_{rate}}^{c_{2Cs}} + c_{3Cs}) \end{aligned} \tag{3.14}$$

$$\begin{aligned} R_1(SOC, T_c, C_{rate}) =& (a_{1Rl} + a_{2Rl}SOC + a_{3Rl}SOC^2 + a_{4Rl}SOC^3 + a_{5Rl}SOC^4) \cdot \left(b_{1Rl}e^{-b_{2Rl}T_c} + b_{3Rl}\right) \\ & \cdot (c_{1Rl} + c_{2Rl}C_{rate} + c_{3Rl}{C_{rate}}^2 + c_{4Rl}{C_{rate}}^3) + d_{1Rl} \end{aligned} \tag{3.15}$$

$$\begin{aligned} C_1(SOC, T_c, C_{rate}) =& (a_{1Cl} + a_{2Cl}SOC + a_{3Cl}SOC^2 + a_{4Cl}SOC^3 + a_{5Cl}SOC^4 + a_{6Cl}SOC^5) \\ & \cdot (b_{1Cl} + b_{2Cl}T_c + b_{3Cl}T_c^2 + b_{4Cl}T_c^3 + b_{5Cl}T_c^4 + b_{6Cl}T_c^5) \\ & \cdot (c_{1Cl} + c_{2Cl}C_{rate} + c_{3Cl}{C_{rate}}^2 + c_{4Cl}{C_{rate}}^3 + c_{5Cl}{C_{rate}}^4) \end{aligned} \tag{3.16}$$

Where T_c is the volumetric average temperature of the battery cell. Values of all coefficient are in appendix.

Considering the dynamic characteristics and application of the battery, the non-linear least squares method is used to identify all the coefficients of ECM parameters. The result comparison of curve fitting and test is shown in Fig.3.6.

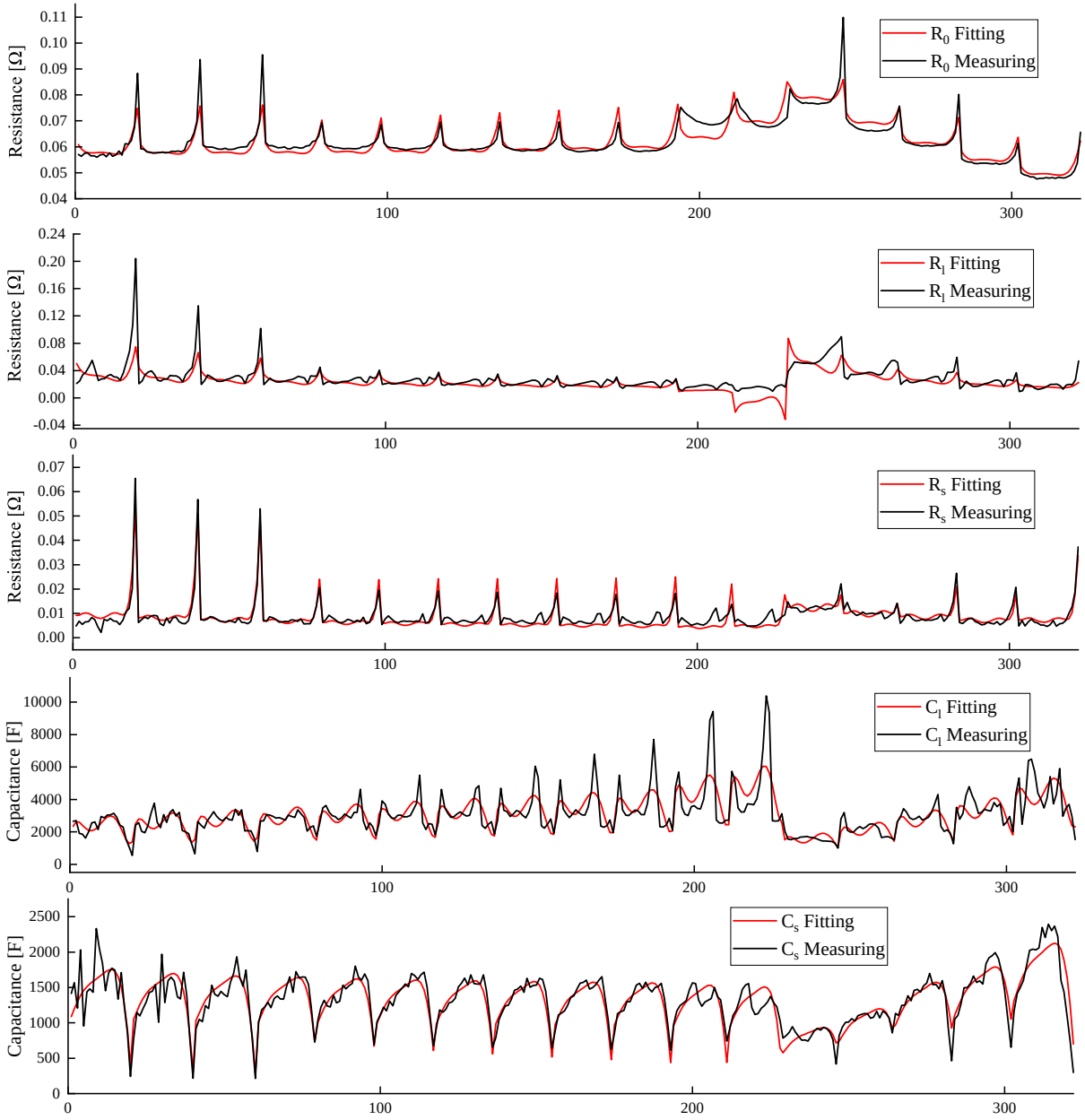

Figure 3.6: ECM parameter curve fitting result based on least squares method (the first 12 cycles were the test sets with C-rate varying from 0.1C to 2.0C and ambient temperature of 25°C; while the the last 5 cycles were the test sets with ambient temperature varying from 0°C to 40°C and C-rate of 0.5C)

The mean absolute percentage error of R_0, R_s, C_s, R_l and C_l are respectively 3%, 21%, 10%, 30% and 18%. The curve fitting is relatively good and can be used for later simulations.

3.2. Thermal Model of Lithium-ion Battery Cell

The thermal model of a single lithium-ion cylindrical battery is essential to understand and manage the thermal behavior of the battery during operation. The model includes the heat generation within the batteries and the heat transfer mechanism within and between the batteries, as shown in Fig.3.8.

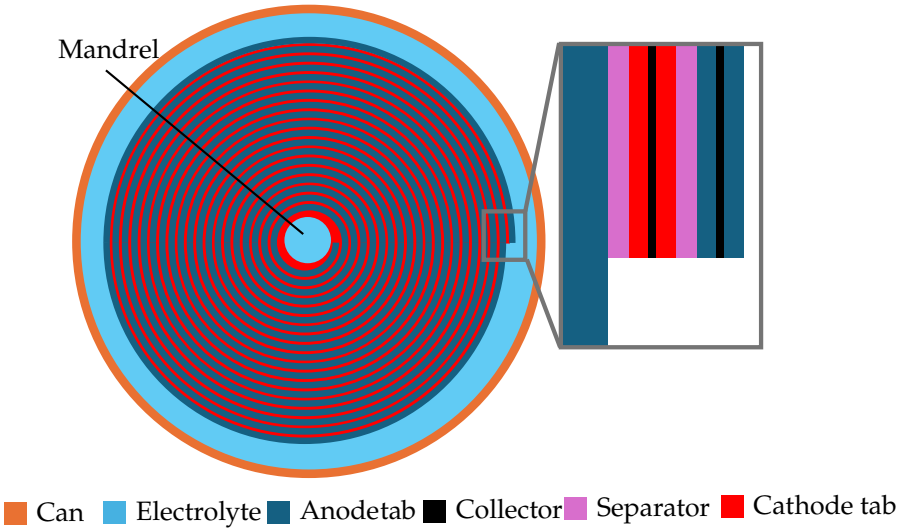

Figure 3.7: Schematic diagram of the cross-section structure of the cell

Spiral electrode assemblies is applied in the Samsung INR 18650-35E battery cell used in this thesis. The main structure consists of 19 turns of tape-shaped electrodes wrapped around the mandrel[40], shown in Fig.3.7. The mandrel shapes and seals the battery cell structure. The anode tape is connected to the edge of the shell, while the cathode tape is located in the middle of the package. During winding, the electrodes are stacked on top of each other with tape-shaped separators between them to prevent short circuit. Both sides of the anode and cathode are coated except for the part of the outermost edge of the anode that is in contact with the package. According to ante-mortem analysis, material composition of the electrodes are Graphite and 1%wt Silicon in anode and $Li(Ni_{0.87}Co_{0.11}Al0.02)O2$ in cathode[41].

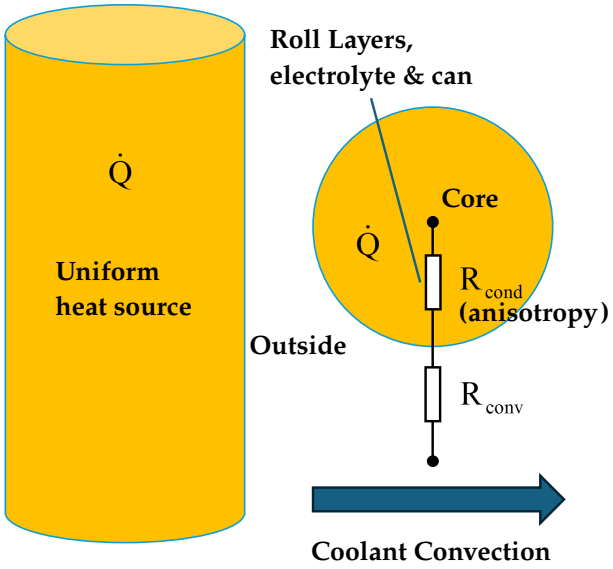

Figure 3.8: Schematic of the thermal model of the battery cell

3.2.1. Heat Generation

To understand the thermal behavior of Li-ion batteries, the rate of heat production inside the battery is crucial. With ECM parameters, the heat generation of the battery cell can also be expressed, as follow[42]:

$$\dot{Q}_c = \dot{Q}_{irrev} + \dot{Q}_{rev} \tag{3.17}$$

$$\dot{Q}_{\text{irrev}} = I^2 (R_0 + R_s + R_l) \tag{3.18}$$

$$\dot{Q}_{\text{rev}} = -IT_c \frac{\partial V_{OC}}{\partial T_c} \tag{3.19}$$

where Q_c is the heat generation of the battery cell, $\dot{Q}_{\text{irrev}}$ is the irreversible heat generation, $\dot{Q}_{\text{rev}}$ is the reversible heat generation. The irreversible heat generation is caused by ohmic heat generation and electrochemical reactions while reversible heat is related to the entropy change due to chemical reactions. According to the V_{OC} experimental results in this chapter, the relationship between V_{OC} and temperature is not obvious, and I is much smaller than I^2, so the reversible heat can be neglected compared with the irreversible heat. The effect of reversible heat is not considered in this thesis. Building an accurate heat generation model in 3D space for different electrochemical properties at each turn of electrodes requires massive computational power. To simplify the model in this thesis, the heat generation within the battery cell is considered to be spatially uniform.

3.2.2. Heat Transfer and Energy Conservation

In the charge and discharge cycle of the LIB, heat is usually conducted inside the battery cell, and transferred between the shell and the outside in conductive or convective way. Based on the available finite element analysis results, it is considered a reasonable assumption to treat the cell of the module as a homogeneous material, but with different thermal conductivity in different directions[43]. In cylindrical coordinate system, the energy balance in the battery cell can be expressed as follows:

$$\rho C_p \frac{\partial T_c}{\partial t} = \frac{1}{r}\frac{\partial}{\partial r}\left(\lambda_r r \frac{\partial T_c}{\partial r}\right) + \frac{1}{r^2}\frac{\partial}{\partial r}\left(\lambda_\phi r \frac{\partial T_c}{\partial \phi}\right) + \frac{\partial}{\partial z}\left(\lambda_z r \frac{\partial T_c}{\partial z}\right) + \dot{Q} \tag{3.20}$$

where ρ is the density, C_p is the specific heat capacity, λ is the thermal conductivity, r, ϕ and z are the cylindrical coordinates.

Due to the large number of interfaces between the electrode and the electrolyte tape in the radial conduction path, there is a difference of nearly two orders of magnitude in the thermal conductivity between the radial and axial directions of cylindrical LIBs. In the three-dimensional simulation of battery heating, the temperature difference in the axial direction is not obvious (<2 °C) as shown in Fig.3.9. Thus, the model is simplified to a two-dimensional model and the axial heat flow is neglected.

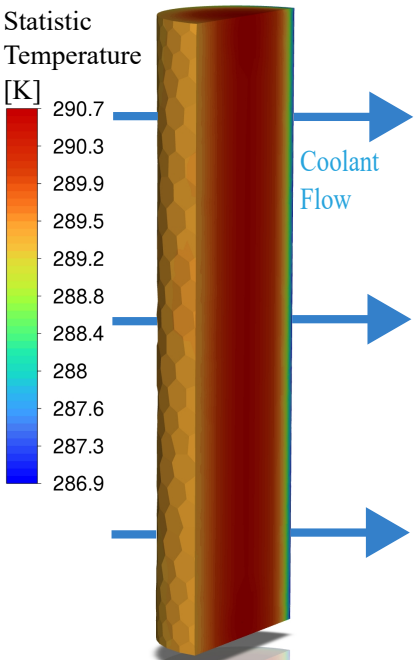

Figure 3.9: Temperature distribution of 3D battery cell model

4

Design of Battery Thermal Management System at Module Level

In the pursuit of high performance battery systems, it is crucial to manage the geometry and thermal environment inside the battery module. BTMS play a key role in maintaining optimal operating temperatures, ensuring safety and extending battery life. This chapter outlines the comprehensive design process of BTMS at the module level, focusing on heat/cooling method, system geometry and configuration, refrigerant control strategy, CFD model construction and simulation result.

4.1. Battery Thermal Management System Selection

The basic requirements of the BTMS include:

- **Stability:** Keeping battery cells within the optimal temperature range
- **Uniformity:** Maintain a uniform temperature distribution within the battery module

Apart form these, additional factors such as weight, size, reliability, and other application-specific requirements of the AEA are taken into account. The most common methods of BTMS design is listed here. Each strategy has its own set of advantages and limitations. Because the mechanism of cooling and heating are similar in the desired condition of BTMS, only the cooling ability of the methods is compared in this thesis.

4.1.1. Air Cooling

Air is not a good cooling medium due to its low heat capacity and low thermal conductivity. However, direct air-cooled BTMS is still a popular solution due to its low cost, stable properties, and simple structure[44].

For aircraft, the direct use of air from external or cabin might not meet the demand. It is often necessary to preprocess the air in some way, such as a vapor compression cycle. Conventional aircraft can use this system to heat air with the heat generated by the gas turbine[45], which cannot be applied to the AEA scenario.

The methods of air cooling are mainly devided to natural convection and forced convection, and the selection depends on the cooling demand. The natural convection of air can only meet the needs of low-density batteries. Other cases require the use of a fan to enhance the convection coefficient. Air has lower heat capacity and lower thermal conductivity than liquid at the same flow rate. Thus, air cooling systems are less effective at keeping the temperature uniform and releasing the large amount of heat generated under high power output of the battery[46]. As a result, in order to ensure performance when using this system, the gap of the battery will be wider, which leads to overall energy density decrease. At the same time, the noise problem caused by the fan is not easy to solve.

4.1.2. Liquid cooling

The ability and performance of liquid cooling systems largely depend on the properties of the coolant, such as viscosity, thermal conductivity, specific heat capacity, density and flow rate. Liquid cooling can be divided into direct cooling and indirect cooling.

Direct Liquid Cooling

Direct liquid cooling, also known as immersion cooling. The cell surface is fully or partially in direct contact with the coolant to minimize thermal resistance in between. Therefore, direct cooling coolants need to be electrically insulating and non-flammable to avoid security risk. Mineral oil and silicone oil are the common choice[47]. Direct liquid-cooled BTMS has not yet been widely used in electric vehicles or aircraft, which may be due to cost and security considerations. And with the high viscosity of mineral oil and silicone oil coolant, additional pumping power is required at the same mass flow rate or volumetric flow rate. Meanwhile, silicone oil has poor thermal conductivity, while mineral oil is volatile and chemically unstable at high temperatures.

Indirect Liquid Cooling

Indirect liquid cooling has good electrical insulation due to the space separation between the battery cell and the cooling channel. This method provides a more reliable and effective heat dissipation solution than air cooling. It performs well in uniform cooling, efficient heat transfer and noise reduction. However, indirect liquid cooling increases the design complexity and maintenance difficulty. Additionally, the increased thermal resistance of the cooling line is a significant consideration.

4.1.3. Phase change materials

Phase change materials have high latent heat. When the battery operates at high power, the PCM melts and absorbs heat. The PCM releases heat to the battery and the environment when the battery is on standby or needs to be heated. If the melting point of the PCM used for thermal management is within the optimal performance range of the LIB, it will be possible to keep the battery temperature at a suitable temperature. PCM does not require any moving parts, which brings low power consumption and maintenance requirements. However, as a passive cooling method, the heat storage capacity of PCM is limited. In the timescale of electric aircraft flight, the PCM may completely melt and lose its cooling capability. At this time, due to its low thermal conductivity, PCM will instead become thermal resistance.

This thesis considers the application of battery pack for AEA. Focusing on the safety of the battery pack and the performance of the BTMS, the characteristics of the above three cooling methods are compared. It is concluded that indirect liquid cooling ensures the electric safety of battery pack, and its cooling effect is sufficient, controllable and easy to maintain. Therefore, indirect liquid cooling is used in the design. In addition, aluminum was selected as the material for the flow channel design due to its good thermal conductivity and low density compared to other support materials[48, 49, 50].

4.2. Geometry of Thermal Management System at Module Level

The battery pack in this thesis is designed by connecting multiple battery modules, which enables a larger scope of modularity than cell level. When AEA is under maintenance on the ground, the number of cells in the current battery pack design may need to be increased to meet the energy requirements of a specific application, or a few cells may need to be replaced. In these cases, modularity can reduce the difficulty of retrofitting. When AEA is in the air, modularity is able to control each battery module independently, reducing the risk of a complete battery pack shutdown in the event of a failure in one or several cells. Meanwhile, with sufficient thermal independence battery modularity reduces the heat exchange between modules, which also reduces the thermal behavior complexity of battery and the burden of BTMS.

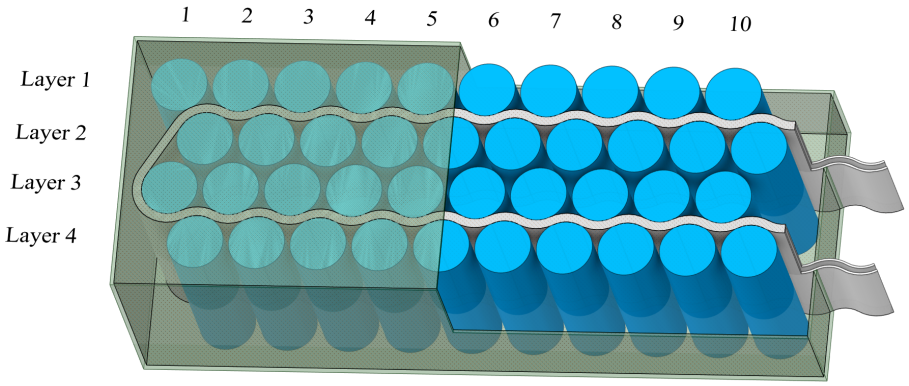

Figure 4.1: Geometry of the battery module

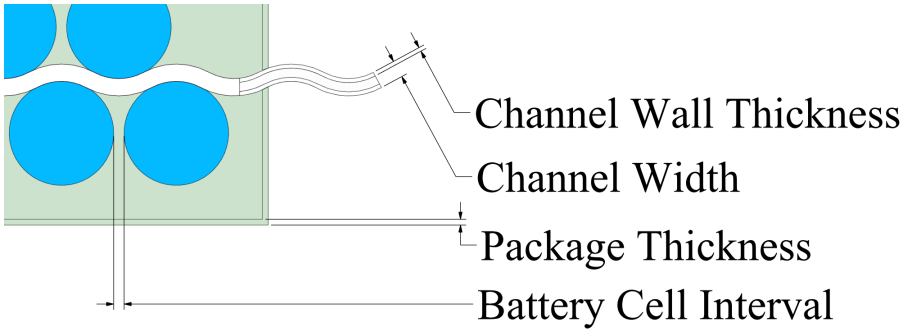

Figure 4.2: Zoomed Geometry of the battery module

Fig.4.1 shows the geometry of the battery module design. BTMS requires uniform cooling of each battery cell under various operating modes and external conditions. For ease of analysis and discussion, the 40 battery cells of the module are numbered. For example, the third cell from the left in layer 2 is numbered 'Cell 2 3'.

Serpentine channel liquid cooling is applied in this thesis. This cooling method is inspired by the battery module used in Tesla Model S and X cars[51]. There is one waveform aluminum cooling/heating channel in each module. Considering the limited cooling ability of a single flow channel, each module is packed with 40 battery cells. The flow channel with a rectangular cross section passes through all cell layers. The height of the channel is the same as battery cell as 65mm. As shown in Fig.4.2, the width and the wall thickness of the flow channel wall determine its shape.

The upper and lower surfaces of the battery are in direct contact with the module package. Each element is fixed at a specific position by a convex groove on the inner surface of the enclosure. The distance between two adjacent cells on the same side of the flow channel is 2mm.

The filling between the battery cell and the flow channel has a flexible and thermal-conductive material. This thermal interface material is graphite sheet material or polymer composite material, which is used to prevent air gaps on imperfect contact surfaces between the element and the flow channel[52]. Due to the large thermal resistance of still air, the existence of air gap will reduce the cooling ability and uniformity of BTMS. The thermal resistance of the thermal interface material is much smaller relative to the other components, so in the thermal model it is neglected.

When the battery temperature rises beyond a certain limit for some reason, a series of chemical reactions will lead to uncontrollable heat release, making the temperature rise further and fall into a vicious cycle. Such a chain reaction will continue and spread in battery modules. This phenomenon is known as thermal runaway. To prevent it from happening, thermal insulation material is used as the cuboid enclosure of the module. The common thermal insulation material parameters are as follows:

Table 4.1: Parameters of most common thermal insulation materials

Material	Density [kg/m^3]	Compressive Yield Strength [MPa]	Thermal Conductivity [mW/(m*K)]
Aerogel	70-110	0.4	29(400°C)
Ceramic thesiss	240-310	0.38-0.47 (60% deflection)	80(400°C)
Ceramic thesiss with Mica Laminate	Thickness dependent		60(400°C)
Flexible Graphite			2800-4500(400°C)
Polyamide thesiss	89-839 [g/m^2]		100(room temperature)

Based on the above parameters, aerogel is selected as the insulating material for the packaging. Aerogel offers excellent thermal insulation properties and a very low density, which significantly reduces the weight and size of the packaging while meeting the required thermal insulation performance. The 1mm aerogel layer was selected as the package for this design because its capability to block the thermal runaway of LIBs has been experimentally verified[53][54].

4.3. Computational Fluid Dynamics Model Construction

CFD method is applied as the conjugate Heat Transfer simulation method in this thesis, in which numerical analysis and data structures is employed to analyze and solve problems related to fluid. ANSYS Fluent software is used to perform the computations necessary for simulating the flow of fluids as well as the interaction between fluids and surfaces defined by boundary conditions. The continuity of fluid is express as:

$$\nabla \cdot \vec{v} = 0 \tag{4.1}$$

where $\vec{v}$ is the vector of fluid velocity.
To determine the state of fluid flow, the Reynolds number is introduce as:

$$\mathrm{Re} = \frac{\rho v d_\mathrm{e}}{\mu} \tag{4.2}$$

where ρ and μ are the density and viscosity of the fluid, d_e is the characteristic length. In this thesis, the characteristic length of the flow is the equivalent diameter(hydraulic diameter) of the channel, which is calculated as,

$$d_\mathrm{e} = \frac{4A}{L} = \frac{2ab}{a+b} \tag{4.3}$$

where A is the cross-sectional area of the channel, L is the wetted perimeter length, a and b are the width and height of the inner sides of the channel. Upon calculation, the Reynolds number in this thesis does not exceed the order of hundreds. The viscous forces significantly outweigh the inertial forces, resulting in a stable, laminar flow. The turbulence intensity is hence set to a very low value to represent fully developed internal flow in the simulation. Within the temperature and pressure ranges considered in this thesis, the fluid is treated as incompressible. Based on the conservation of momentum and mass, the N-S(Navier-Stokes) equations is as follow:

$$\frac{\partial \vec{v}}{\partial t} + \left(\vec{v} \cdot \nabla\right) \vec{v} = g + f - \frac{\nabla p}{\rho} + \frac{\mu}{\rho} \nabla^2 \vec{v} \tag{4.4}$$

where g and f are the gravitational and external force acceleration, p is the static pressure. The energy balance of the fluid is represented as follows:

$$\rho C_\mathrm{p} \left(\frac{\partial \mathrm{T}}{\partial \tau} + u \frac{\partial \mathrm{T}}{\partial x} + v \frac{\partial \mathrm{T}}{\partial y} + w \frac{\partial \mathrm{T}}{\partial z} \right) = \lambda \left(u \frac{\partial^2 \mathrm{T}}{\partial x^2} + v \frac{\partial^2 \mathrm{T}}{\partial y^2} + w \frac{\partial^2 \mathrm{T}}{\partial z^2} \right) + \dot{Q} \tag{4.5}$$

Due to the low velocity and incompressibility of the fluid, a type of pressure-based methods (segregated methods), Semi-Implicit Method for Pressure-Linked Equations (SIMPLE), is employed in this study.

The process is illustrated in Fig.4.3, where the control equations for each variable are decoupled from the solutions of other equations during the solving procedure.

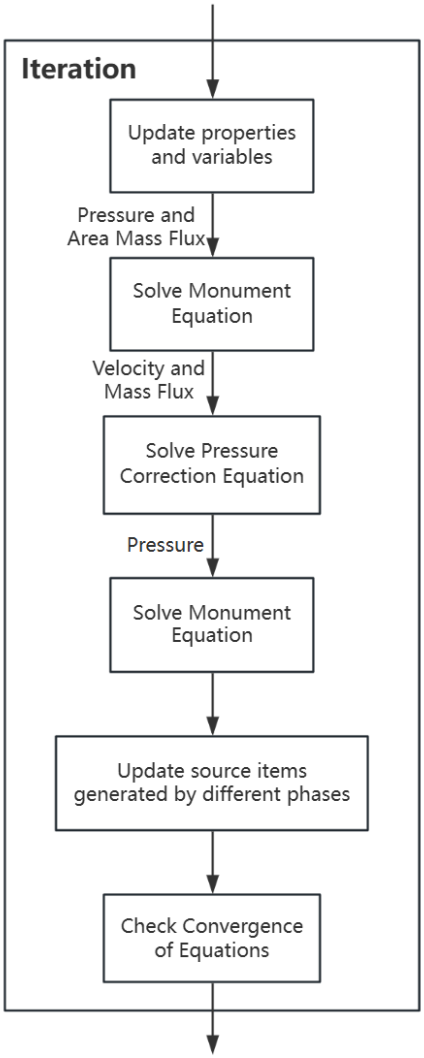

Figure 4.3: Flowchart of the SIMPLE method

Given the complexity of the model's geometry, which involves a significant number of unstructured grids, the distance-based Rhie-Chow method is employed. This approach improves the coupling between pressure and velocity fields through interpolation, thereby reducing discretization errors and avoiding numerical oscillations. For the same reason, least squares cell based method is employed to solve for the gradients of the flow field variables.

4.3.1. Basis Initial and Boundary Conditions

To simplify the calculation, the following assumptions are made in this thesis:

- Initially, the cell, coolant, channel, package, and air in all voids were at a uniform temperature of 298K. The battery is fully charged (SOC=100%).
- The power load of the battery in the process only changes with time, and its numerical profile is shown in Fig.2.1.
- The outer surface of the battery module package is assumed to have sufficient heat exchange with the external environment, and its temperature is regarded as consistent with the external temperature, which only changes with time.

- The interfaces between the coolant and the channel, and between the channel and the cell are regarded as a well-contacted interface, which means that the temperature and heat flux are spatially continuous.
- The temperature is considered to be continuous in time. The volume average temperature (area average temperature in 2D) of each battery is regarded as the battery temperature. The heating rate of each battery at each time is obtained by solving the ECM in Chapter.3.
- The velocity inlet characterizes the turbulent state with a turbulence intensity of 5% and the corresponding hydraulic diameter calculated by Eq.4.3.

4.3.2. Mesh Independence Verification of Computational Fluid Dynamics Model

From the perspective of finite element analysis principles, finer mesh discretization generally results in higher solution accuracy. However, in practical engineering applications, a dramatic increase in the number of mesh significantly raises computational time costs. Moreover, beyond a certain mesh density, the improvement in computational accuracy becomes marginal and may even lead to increased error accumulation. Therefore, it is necessary to identify the minimum mesh density required to achieve sufficient accuracy of CFD simulation.

This study simulates models with mesh quantity ranging from 10,000 to 210,000 elements. The mesh characteristics within each component of the module are maintained, while the mesh size is adjusted to achieve an exponential increase in the number of mesh.

In order to judge the accuracy of simulation results with different grid densities more easily, the complexity of case should be reduced. So the basis initial and boundary condition is simplified further: The outer surface of the module is set to be adiabatic and no external refrigerant is input, so that the impact of the BTMS and external temperature is excluded. It was observed that the maximum temperature of each battery cell within the module occurs at the same time point (the end of the climb procedure of the flight). This temperature maximum value is used to evaluate the accuracy of the mesh simulation results, as illustrated in the Fig.4.4.

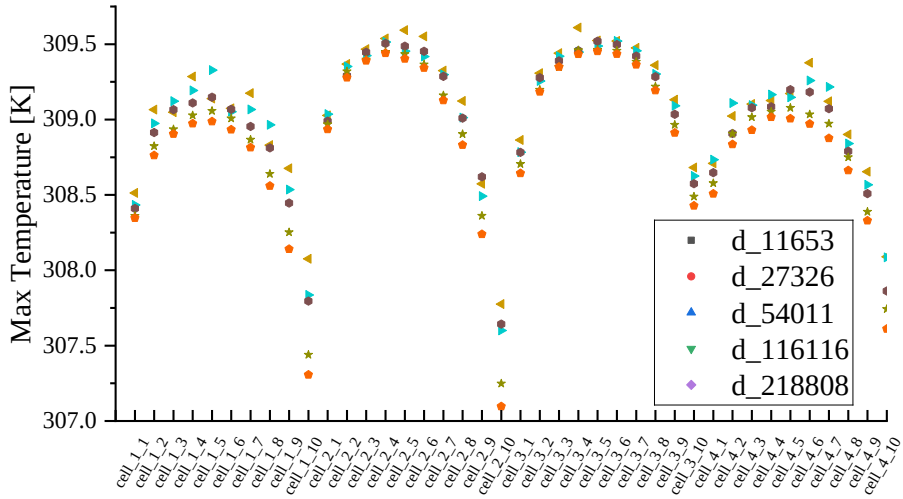

Figure 4.4: Maximum temperature comparison in each cell with different mesh quantity

The results show that as the number of mesh increases, the data trends remain generally consistent. Considering the spatial structure of the battery module, the continuous spatial arrangement of similarly cooled cells within the same battery layer should lead to temperature continuity. Thus, it is determined that simulations with more than 110k mesh elements are reasonably accurate. Numerically, the difference between the results for 110k and 200k mesh elements is less than 0.4%, indicating that the simulation results have converged when the mesh quantity reaches 110,000. Therefore, the model with 110k mesh is used for subsequent simulations.

Property	Air	Mineral oil	Silicone oil	Water
Density [kg·m^3	1.225	924.1	920	998.2
Specific heat capacity [J/(kg·K)]	1006	1900	1370	4182
Thermal conductivity [W/(m·K)]	0.0242	0.13	0.15	0.0242
Kinematic viscosity [m^2/s]	1.46e-5	5.60e-5	-	0.898e-6

Table 4.2: The thermal properties of normal refrigerant

4.4. Refrigerant Control Strategy

The normal refrigerant are air, liquid and the thermal properties are shown in Table.4.2.

As one of the most effective coolants in a variety of industrial applications and with low kinematic viscosity and high specific heat capacity, water is chosen as the coolant in this design.

When the system reaches the steady state, the coolant flow velocity could be calculated as:

$$v_{\mathrm{st}} = \frac{\dot{Q}_{\mathrm{m}} N}{\rho_{\mathrm{l}} C_{\mathrm{pl}} \Delta T_{\mathrm{l}}} \tag{4.6}$$

where v_{st} is the steady flow velocity requirement of refrigerant, $\dot{Q}_{\mathrm{m}}$ is the net heat input to the battery module, N is the number of battery cells in a module, ρ_{l} and C_{pl} are the density and the specific thermal capacity of refrigerant, ΔT_{l} is the temperature difference of the refrigerant at channel inlet and outlet.

But in fact, the temperature change of the working fluid is an unbalanced transient process. Therefore, in the transient simulation, in order to achieve temperature uniformity and stability, BTMS monitors the volumetric average temperature of each cell in real time. Moreover, since the average temperature of all cells is not representative for the most extreme cell temperature case, the average of the highest and lowest cell temperatures is used instead as the basis temperature for deciding the BTMS mode in this design, in order to control the temperature of all batteries within appropriate range.

$$T_{\mathrm{b}} = \frac{1}{2} \left(T_{\mathrm{c,max}} + T_{\mathrm{c,min}} \right) \tag{4.7}$$

where T_{b} is the basis battery cell temperature.

In this thesis, the target cell temperature of the battery is set to 298K (25°C), where the cell simultaneously has a high discharge capacity and a long cycle life. For the stability of cell temperature, the rate and temperature of the input refrigerant to the BTMS will be determined by the required heat transfer load. Therefore, it is necessary to decide which parameter is the control variable of BTMS and which stays constant. There are three options:

Constant Temperature and Variational Flow Rate: Keeping the temperature of the refrigerant constant means stable heat transfer performance. Because in the process of heat exchange, a stable temperature difference provides a stable heat transfer rate. The adjustment of the flow rate is realized by the adjustment of the pump or valve. To avoid excessive heat transfer, the flow rate should be controlled accurately and quickly. So the pump needs fair variable-speed adjustment ability.

Constant Flow Rate and Variational Temperature: When the flow rate is kept constant, the control of the pump for the refrigeration cycle is relatively simple. The control of the temperature change of the refrigerant can flexibly control the cooling capacity and heat supply, which can be realized by adjusting the compressor or throttle valve of the refrigeration cycle. Nonetheless, temperature regulation requires accurate cooling capacity control, which usually requires the addition of more complex temperature regulation equipment and control algorithms in the refrigeration cycle.

Variational Temperature and Flow Rate: In theory, adjusting the temperature and flow rate simultaneously is the most flexible method. However, the need for additional equipment greatly increases the complexity and maintenance difficulty of the system.

In summary, the refrigerant control with constant temperature and variatianal speed is the best selection to achieve stable battery cell temperature. The constant refrigerating temperature of the refrigerant is set as 293K (20°C), and the constant heating temperature of the refrigerant is set as 303K (30°C). And the simulated flow rate control strategy is set as follow:

4.4.1. Constant Flow Rate Control

Setting flow rate as a constant is the most simple way of refrigerant flow rate control. Considering that constant flow rate control would not be the optimal choice for this design, so the simulation goal for this method is to observe its characteristics and performance. Based on this reason, several attempts were made as follow:

The inlet flow velocity of this control strategy is fixed to a relatively high value of $0.02\mathrm{m/s}$ for large temperature variations during simulation, expecting more obvious characteristics of thermal control performance.

$$v_{\mathrm{in}} \equiv 0.02 \tag{4.8}$$

where v_{in} is the flow velocity of input refrigerant.

It can be expected that because the flow velocity is always constant and greater than v_{st}, the battery basis temperature will not stabilize at the target temperature, but will frequently fluctuate up and down around the target temperature. In order to prevent unrealistically frequent switching between heating and cooling level of inlet refrigerant temperature, mode switch is triggered only when the basis temperature deviates from the target temperature 298K (25°C) by no less than 3K. In the case that this condition is not met, the thermal management mode remains unchanged:
When $T_{\mathrm{b}} - 301 > 0$, $T_{\mathrm{cool}} = 293$;
When $T_{\mathrm{b}} - 295 < 0$, $T_{\mathrm{heat}} = 303$.

During the simulation time, the cell to cell maximum difference was monitored as well to evaluate the uniformity of thermal control.

4.4.2. Proportional (Linear) Flow Rate Control

Linear control is a simple temperature-based control method, which is to make the flow rate of the working fluid linearly dependent on the basis temperature of the battery. The flight process in this thesis does not have extreme dynamic characteristics, so the method is expected to achieve good thermal stability. For proportional control, because the system of the module is not a thermal closed system, the offset(steady-state error) must exist. Therefore, a constant term is added to the governing equation to eliminate part of the offset:
When $T_{\mathrm{b}} - 301 > 0$, $v_{\mathrm{in}} = 0.005\,(T_{\mathrm{b}} - 301) + 0.005$;
When $T_{\mathrm{b}} - 295 < 0$, $v_{\mathrm{in}} = 0.005\,(295 - T_{\mathrm{b}}) + 0.005$.

4.4.3. PD Flow Rate Control

PD control consists of proportional control and differential control. Compared with Proportional (Linear) Flow Rate Control, PD control can quickly respond to input changes. Especially in the dynamic process of the system, differential control can predict the change trend of the error, make adjustments in advance, and reduce the response time. At the same time, the differential control part can effectively suppress the overshoot of the system and reduce the oscillation or overshoot phenomenon. However, differential control adjusts the rate of change of the error, so it is sensitive to high-frequency noise. The PD control simulated in this thesis is as:
When $T_{\mathrm{b}} - 301 > 0$, $v_{\mathrm{in}} = 0.005\,(T_{\mathrm{b}} - 301) + 5\frac{\delta T_{\mathrm{b}}}{\delta t} + 0.005$;
When $T_{\mathrm{b}} - 295 < 0$, $v_{\mathrm{in}} = 0.005\,(295 - T_{\mathrm{b}}) - 5\frac{\delta T_{\mathrm{b}}}{\delta t} + 0.005$.

4.4.4. Simulation Result

At the beginning of the simulation, the time of the initial refrigerant flowing through the whole channel is affected by the velocity. In order to better compare the two cooling methods, this part of the influence needs to be eliminated. Therefore, the initial refrigerant temperature in the flow channel is set to 293K in this simulation.

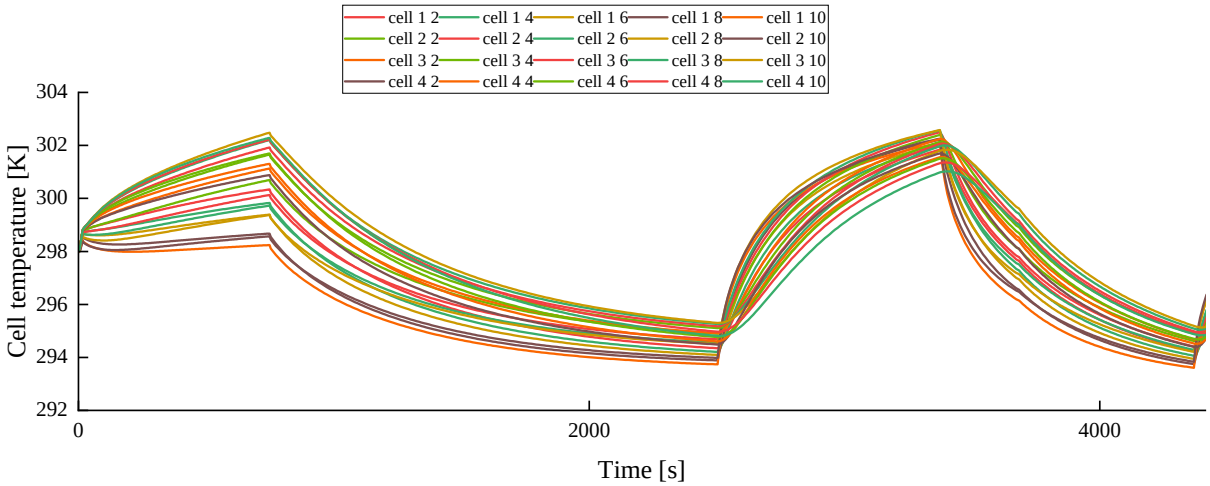

Figure 4.5: Cell temperature with constant flow rate control

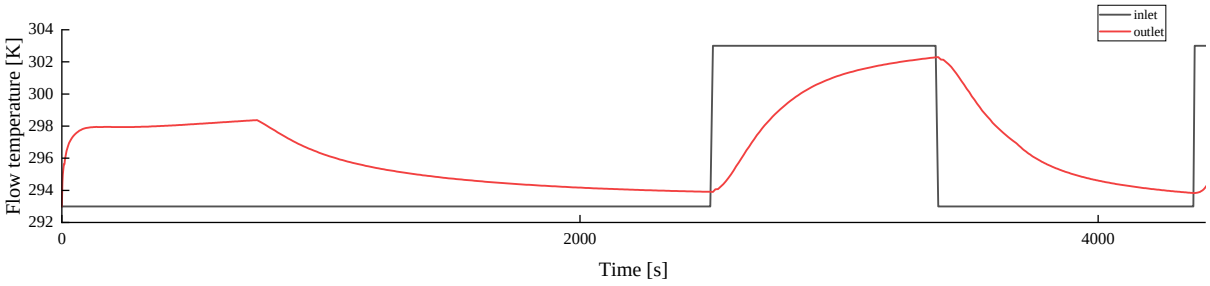

Figure 4.6: Flow temperature with constant flow rate control

The cell temperature and the flow temperature variation with constant flow rate control are shown in Fig.4.5 and 4.6. The cell to cell maximum difference is 4.1K. The highest temperature is 302.3K at 752s (the end of the climbing phase). The lowest temperature is 294.0K at 2493s. The piecewise analysis of the mechanism is as follows:

It is observed that the battery cell temperature and the refrigerant outlet temperature during take-off and climb process rise with time. This is because the cell volumetric heat generation is at a high level during this time, so the refrigerant is only able to slow down but not stem the increase in cell temperature. At the same time, the rising temperature of the cell increases the heat transfer between the cell and the refrigerant. This causes the temperature difference between the highest (at outlet) and the lowest (at inlet) of the refrigerant in the entire flow channel to increase with time. And the spatial uniformity of the temperature difference between every cell and the refrigerant in adjacent position of cell decreases with time. The consequence is that the temperature range of all batteries increases with time.

Since the beginning of the cruise process, it is observed that the cooling and heating state switch occurs three more times during the flight. The cooling and heating effects are significant. The mechanism is similar to the mechanism of take-off and climbing process, except that the heat dissipation of BTMS and the battery exceeds the heat dissipation of the battery in the cooling process, and the heat supply of BTMS and the battery exceeds the heat dissipation of the outside world in the heating

process. Under the influence of a large flow rate, the refrigerant provides excessive heat transfer, so the battery module frequently switches between cooling and heating, which means unnecessary heat transfer energy consumption.

It can be observed that in a single cooling or heating process, at the instant of mode switching, the refrigerant temperature change along the channel reaches the maximum value, and then the refrigerant outlet temperature always approaches the inlet temperature. This is because in the heat transfer process, as the temperature of each cell gradually approaches the temperature of the refrigerant in adjacent position of the cell, the heat transfer between them decreases with time. So the temperature change of the refrigerant after flowing through the whole flow channel decreases with time. This also leads to a more uniform heat transfer of the refrigerant to the battery cell along the whole flow channel, so that the temperature range of the battery cells is reduced with time.

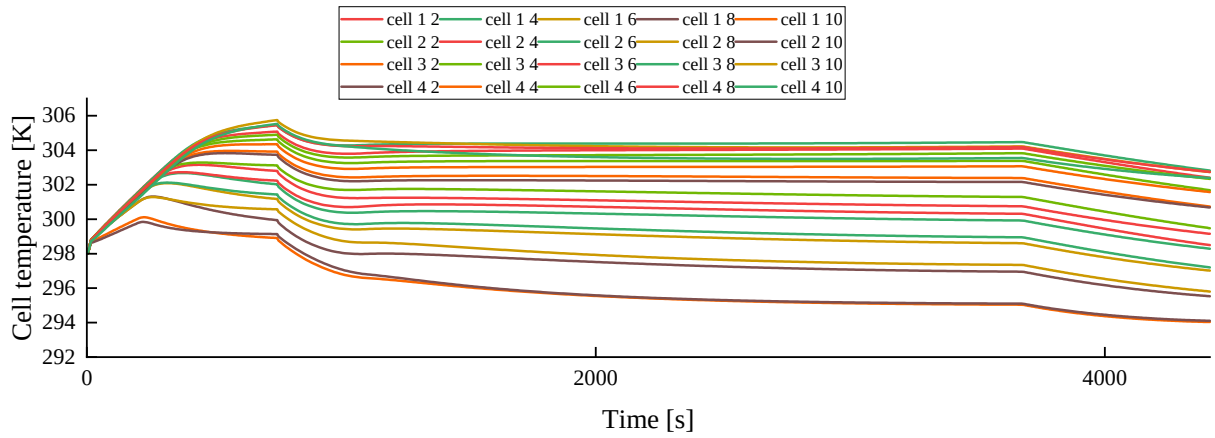

Figure 4.7: Cell temperature with linear flow rate control

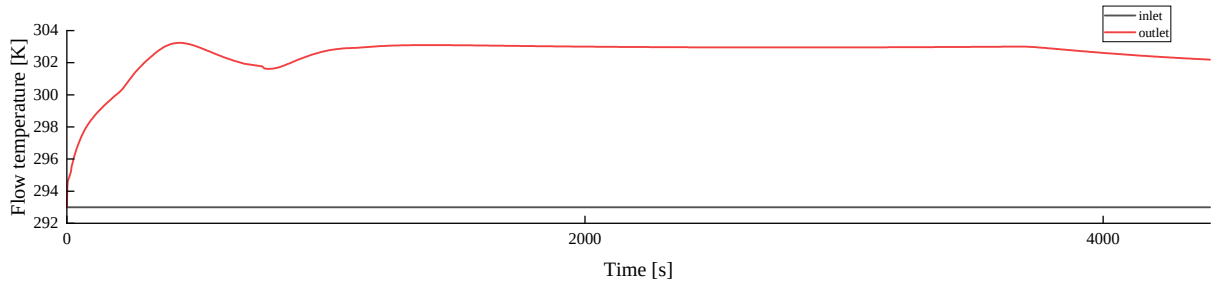

Figure 4.8: Flow temperature with linear flow rate control

The cell temperature and the flow temperature variation with linear flow rate control are shown in Fig.4.7 and 4.8. The cell to cell maximum difference is 9.4K. The highest temperature is 305.7K at 752s (the end of the climbing phase). The lowest temperature is 294.1K at 4413s. Compared with the constant flow rate control, the average velocity of the linear flow rate control is much smaller. The temperature change of the battery tends to be stable during the whole flight, and this control strategy meets the requirement of keeping battery cells in the optimal temperature range. However, due to the always large temperature difference between the inlet and outlet of the working flow, the temperature difference between the battery cells in this process exceeds 8K, which is unacceptable.

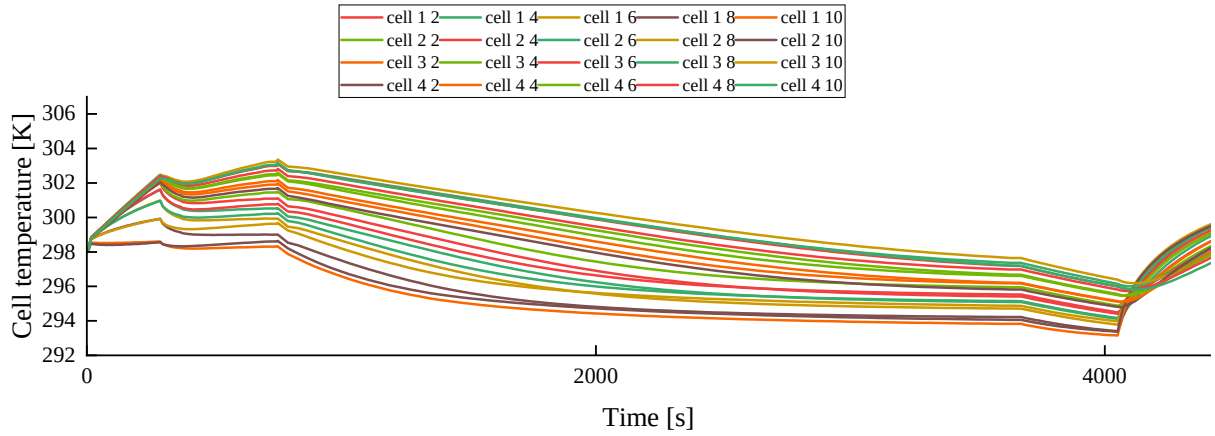

Figure 4.9: Cell temperature with PD flow rate control

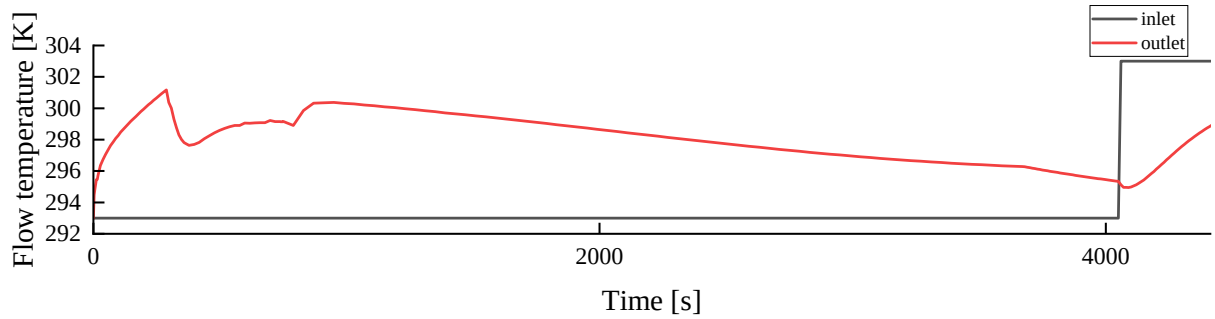

Figure 4.10: Flow temperature with PD flow rate control

The cell temperature and the flow temperature variation with PD flow rate control are shown in Fig.4.9 and 4.10. The cell to cell maximum difference is 6.2K. The highest temperature is 303.2K at 752s (the end of the climbing phase). The lowest temperature is 293.2K at 4050s. PD flow rate control only adds differential control to linear flow rate control. Observing the battery temperature curves during climbing, it can be found that the differential control accelerates the response speed of the system, and the trend of temperature rise is quickly contained. The refrigerant temperature difference between the inlet and outlet during the flight is between the constant flow rate control and the linear flow rate control.

During the flight, the thermal uniformity and thermal stability of the battery reached a balance, and both were relatively good. Thus, this design selects PD flow rate control as BTMS control strategy.

4.5. Geometry Optimization

The BTMS system needs to control the temperature of the LIB in the optimal operating temperature range of 20 to 40°C, while maintaining the maximum temperature difference between the cells below 5 °C[55]. However, the thermal performance of the battery module and the power consumption of the BTMS are often promoted simultaneously. In this thesis, we consider minimizing the BTMS power consumption during a scheduled flight while meeting the thermal performance target of the battery module. Therefore, it is necessary to optimize the various parameters of the battery module. The design prioritizes optimizing the energy consumption of BTMS and the energy density of the battery module. To achieve this, some key geometric parameters that significantly influence these factors are selected for optimization: the interval between adjacent cells, the thickness of the flow channel wall, and the thickness of the outer packaging of the module.

In order to amplify the difference in thermal performance of the battery module with different battery intervals, the constant flow rate control mentioned above is selected as the refrigerant control

strategy in this simulation to increase the temperature variation. Cell 1 1 with the smallest contact area with the flow channel, Cell 1 10 near the entrance and not surrounded by other cells, and Cell 3 10 near the exit and surrounded by other cells are selected as the observation objects.

4.5.1. Battery Cell Interval

The effect of 1mm, 2mm, 4.5mm and 7mm cell spacing on the thermal performance of the battery module was studied. Since the upper and lower surface area of the flow channel is much smaller than the side area of the flow channel, it can be considered that when the thickness of the channel stays the same, the volume and mass of the flow channel are directly proportional to the side area of the flow channel. The utilization ratio of the flow channel side area can be obtained:

$$\eta = \frac{A_{\text{con}}}{A_{\text{tot}}} \tag{4.9}$$

where η is the utilization ratio of the flow channel side area, A_{con} is the contact area between the flow channel side and the battery cell side, A_{tot} is the total area of the flow channel side.

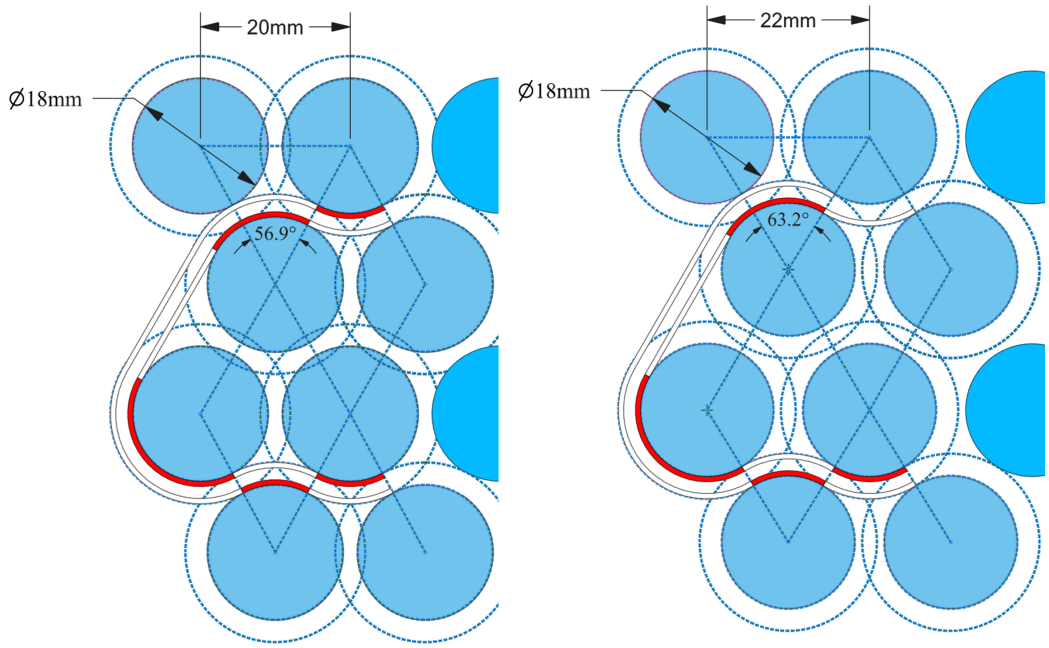

Figure 4.11: Geometric constraints on the shape of the flow channel with 2mm and 4.5mm battery cell interval (the contact surface is marked in red)

The constraints to construct the flow channel geometry are shown in Fig.4.11 for the example of 2mm cell interval. From the exact geometry, the volume of cell, channel, flow and package within a single module can be calculated, and thus the weight of the module can be obtained:

$$M_{\text{m}} = \sum \rho_{\text{i}} Vol_{\text{i}} \tag{4.10}$$

where M_{m} is the total mass of the module, ρ is the material density of every component, Vol is the volume of every component.

In general, the specific heat capacity is a function of temperature. However, considering that the temperature variation range of the refrigerant through the whole flow channel is minor, the specific heat capacity can be approximated to a constant. Therefore, the heat transfer of the refrigerant to battery module is calculated as follows:

$$\begin{aligned} Q_{\mathrm{ht}} &= \rho_{\mathrm{l}} C_{\mathrm{pl}} \int q_{\mathrm{v}} \left(T_{\mathrm{out}} - T_{\mathrm{in}}\right) dt \\ &= \rho_{\mathrm{l}} C_{\mathrm{pl}} A_{\mathrm{in}} \int v_{\mathrm{in}} \left(T_{\mathrm{out}} - T_{\mathrm{in}}\right) dt \end{aligned} \tag{4.11}$$

where Q_{ht} is the heat transfer between refrigerant and battery module, q_{v} is the volume flow rate of refrigerant, A_{in} is the cross-sectional area of the flow channel inlet.

The models are constructed separately according to the same channel geometric constraints to maximize the utilization ratio of the flow channel side area, which is to minimize the weight of BTMS. As can be inferred: When the battery cell interval increases, the angle of each arc forming the flow channel shape also increases. As a result, the contact area between one cell and the flow channel increases, while the utilization ratio of the flow channel side area decreases. The former accelerates the heat transfer effect of BTMS, while the latter lowers the energy utilization of BTMS. Because the lower utilization ratio of the flow channel side area means that the ineffective heat transfer of the flow channel to the air increases.

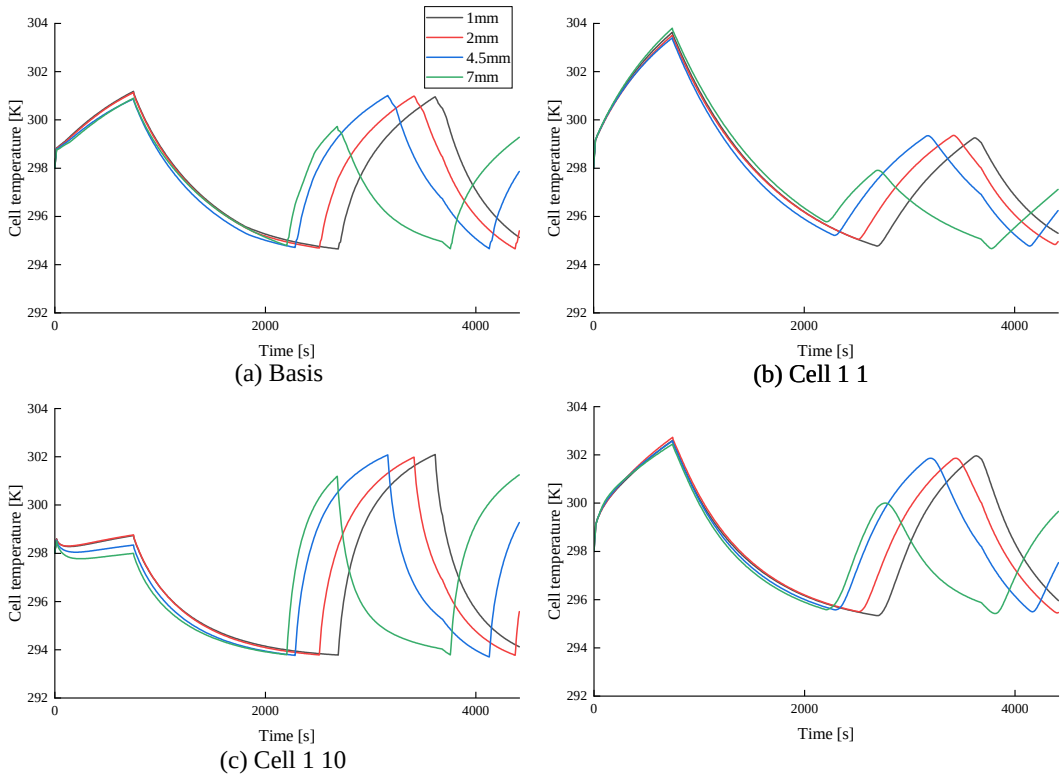

Figure 4.12: Variation of basis and 3 typical cell temperature at different battery cell interval: (a) The basis temperature (average of maximum and minimum cell temperature) (b) The cell with the worst heat transfer to the flow channel; (c) The cell with the best heat transfer to the flow channel; (d)The cell with poor heat transfer to the flow channel and surrounded by other cells

The simulation result is shown in Fig.4.12. Consistent with the previous conjecture, the cooling and heating rates of all stages increase with the increase of the battery interval. Therefore, the temperature curve of the larger cell interval has the same shape as that of the smaller cell interval, except that it shrinks in equal proportion in the horizontal direction.

With Eq.4.11, the energy consumption in the first period of cooling and the first period of heating are calculated. And with Eq.4.10, the mass energy density is calculated. Since the total energy of the

Table 4.3: Comparison of simulation results calculation for different battery cell intervals

Battery Cell Interval [mm]	1	2	4.5	7
Heat Transfer Energy (cooling) [Wh]	17.68	17.23	16.80	16.79
Heat Transfer Energy (heating) [Wh]	6.49	6.47	6.70	5.90
Heat Transfer Energy (sum) [Wh]	24.17	23.70	23.50	22.70
Mass Energy Density [Wh/kg]	221.40	220.44	218.04	215.58
Volumetric Energy Density [kWh/m^2]	394.39	376.02	336.95	305.68

battery module maintains, the volumetric energy density of the module is inversely proportional to the module volume. These result are shown in Table.4.3

Considering the energy consumption and module energy density, this design chooses 2mm battery cell interval.

4.5.2. Channel Wall Thickness

The influence of 0.4mm, 0.7mm and 1.0mm channel wall thickness on the thermal performance of the module is studied. Because the flow channel wall material is aluminum, which is an excellent thermal conductivity material, its thermal resistance can be ignored in the heat transfer process between the refrigerant and the battery. The thickness of the flow channel wall is predicted to have little influence on the thermal performance of BTMS.

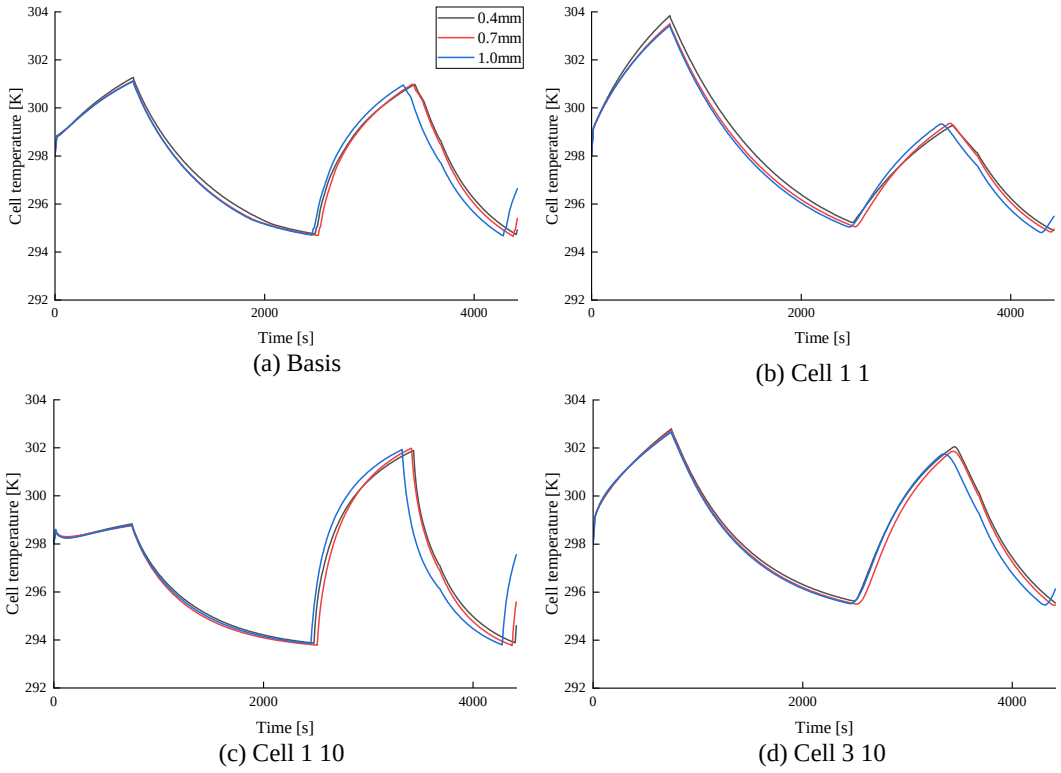

(a) Basis (b) Cell 1 1

(c) Cell 1 10 (d) Cell 3 10

Figure 4.13: Variation of basis and 3 typical cell temperature at different channel wall thickness: (a) The basis temperature (average of maximum and minimum cell temperature) (b) The cell with the worst heat transfer to the flow channel; (c) The cell with the best heat transfer to the flow channel; (d)The cell with poor heat transfer to the flow channel and surrounded by other cells

As shown in Fig.4.13, different thickness of the flow channel has a very limited impact on the thermal performance of the battery module. In order to pursue the maximum battery mass energy density with enough structural strength, the flow channel of 0.4mm is selected in this thesis.

Table 4.4: Comparison of simulation results calculation for different channel wall thickness

Channel Wall Thickness [mm]	0.4	0.7	1.0
Heat Transfer Energy (cooling) [Wh]	17.13	17.23	17.19
Heat Transfer Energy (heating) [Wh]	6.18	6.47	6.67
Heat Transfer Energy (sum) [Wh]	23.32	23.70	23.80
Mass Energy Density [Wh/kg]	226.04	220.44	215.11
Volumetric Energy Density [kWh/m^2]	382.09	376.02	370.18

4.5.3. Package Thickness

The effect of 0.5mm, 1.0mm and 2.0mm package wall thickness on the thermal performance of the module is studied. The larger packing thickness can better isolate the battery module from the external heat exchange. Considering that during the flight in this thesis, the outside temperature is always lower than the battery temperature, so the battery module dissipates heat to the outside during the whole process. It is predicted that a larger packing thickness will slow down the cooling process and speed up the heating process of BTMS.

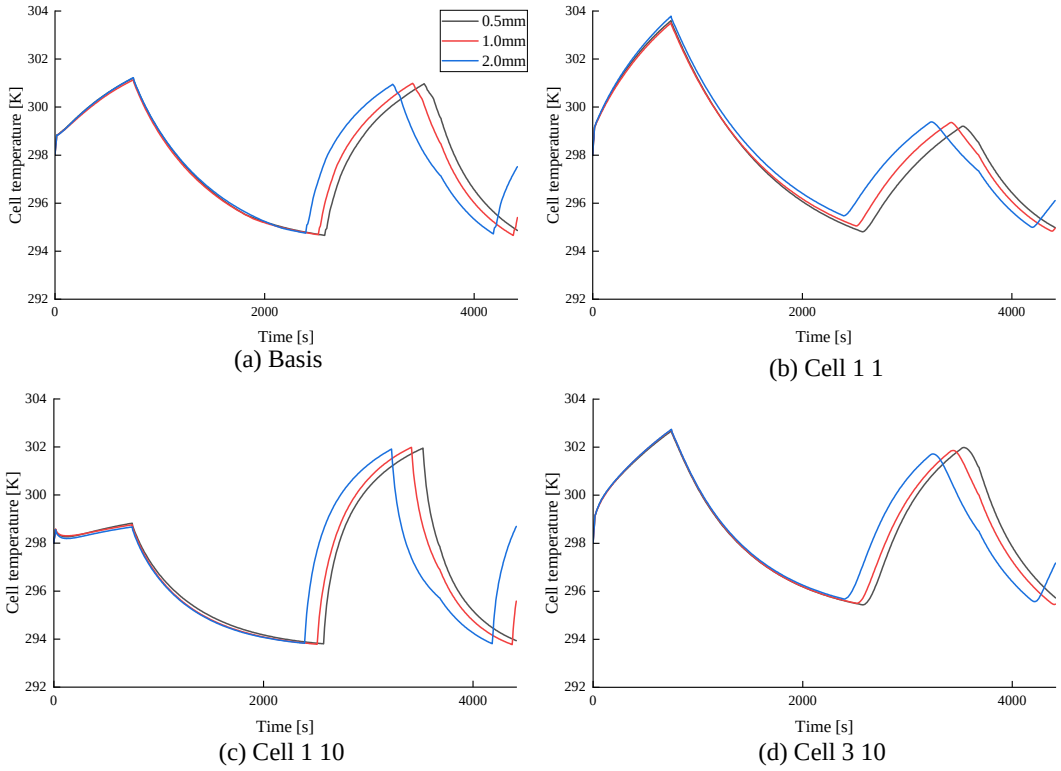

(a) Basis (b) Cell 1 1

(c) Cell 1 10 (d) Cell 3 10

Figure 4.14: Variation of basis and 3 typical cell temperature at different package thickness: (a) The basis temperature (average of maximum and minimum cell temperature) (b) The cell with the worst heat transfer to the flow channel; (c) The cell with the best heat transfer to the flow channel; (d)The cell with poor heat transfer to the flow channel and surrounded by other cells

The result is shown in Fig.4.14. The larger package thickness compared with the smaller package thickness, the curve of the cooling part lengthened in equal proportion in the horizontal direction, and the curve of the heating part shortened in equal proportion in the horizontal direction.

As can be seen in Table.4.5, the larger packaging thickness reduces the total energy consumption of BTMS, but also reduces the bulk energy density of the battery module at the same time. Balancing the two, 1mm packing thickness is selected in this thesis.

Table 4.5: Comparison of simulation results calculation for different package thickness

Channel Wall Thickness [mm]	0.5	1.0	2.0
Heat Transfer Energy (cooling) [Wh]	17.21	17.23	17.29
Heat Transfer Energy (heating) [Wh]	6.68	6.47	6.23
Heat Transfer Energy (sum) [Wh]	23.89	23.70	23.52
Mass Energy Density [Wh/kg]	220.67	220.44	219.99
Volumetric Energy Density [kWh/m^2]	382.15	376.02	364.21

4.5.4. Conclusion

Based on the above simulation results, the energy consumption of the BTMS system and the energy density of the battery module are balanced, and structural strength restriction is considered. The optimization battery module with 2mm cell spacing, 0.4mm flow channel wall thickness, 1mm packaging thickness, and constant flow rate control to have the best temperature characteristics and lowest energy consumption. The external dimension of the module is determined to be 222mm×88mm×67mm. The weight ratio of the BTMS in battery module is 5.99%.

5

Thermal Performance of Battery Pack

Compared to a single battery module, a battery pack contains a combination of multiple battery modules, so the complexity and importance of its thermal management increases accordingly. In large battery packs, thermal management systems must consider heat transfer between multiple modules, heat uniformity, and the potential risk of thermal runaway.

5.1. Module to Pack Structure

To design the battery pack, the location of its placement should be determined first. The distribution of the battery pack in AEA in this design is inspired by the fuel tank distribution in conventional aircraft. Conventional passenger aviation designs used to place fuel tanks on the wings, known as wet wing technology. This technology has been popularized in large conventional passenger aircraft, small general aviation aircraft, and some military transport aircraft. It is also very valuable in the design of a AEA battery pack with several advantages:

- In terms of the load reduction, If the battery pack is stored in a separate area within the fuselage, additional support structures, partitions, and protective shell will be required to isolate it from the rest part of the fuselage. By contrast, wet wing technology directly utilizes the internal structure of the wing as storage space, eliminating the need for separate storage area and thus reducing the weight of the aircraft.
- In terms of the load distribution, placing more weight on the wing can reduce the weight of the fuselage and avoid excessive deformation of the wing near the fuselage due to large torque.
- In terms of space utilization, the wet wing maximizes the structural volume available within the wing.
- In terms of the safety, the battery pack located outside the passenger compartment prevent the high-voltage components of battery pack from posing any threat to passengers. And convective heat dissipation from external high-speed air can also reduce chain overheating between modules in the event of thermal runaway.

In order to maximize the space usage inside the wing and balance the weight distribution, all the battery packs are in the same horizontal plane and there is no stacking in the altitude or front direction. It also eliminates the need for additional structural support for multi-tier configurations.

Because each battery management system is only able to monitor a limited number of cells, the total number of cells within a single battery pack is limited. By design, 8 rows, 3 columns, and 1 layer of modules are distributed in each battery pack, with 40 cells in each module. Each battery module has its corresponding stationary frame, electrical connection device, as well as temperature sensor, voltage detection circuit, etc. This single layer distribution is selected to perform better thermal uniformity of the modules within the battery pack than multi-layer distribution, since thermal accumulation between layers is avoided.

In order to cope with the possible battery expansion requirements, the connection between battery modules has also been modularized to a certain extent. One battery pack is composed of repeated structures next to each other arranged in the vertical direction, and the smallest repeated structure is two rows with a total of six modules, which is shown in Fig.5.1. The connection between these two rows of modules is the flow channel and the connecting circuit. The inlets and outlets of each module are connected and then lead to the cooling and heating system through the passages on the side of the battery pack (in the fireproof layer). This structure obtains a smaller total length of the flow channel and wire. A smaller channel length leads to a shorter flowing path of refrigerant from the refrigeration cycle to the cell, which causes a faster control response of the BTMS. The resistance loss of the wire decreases with the total length, which can improve the system efficiency.

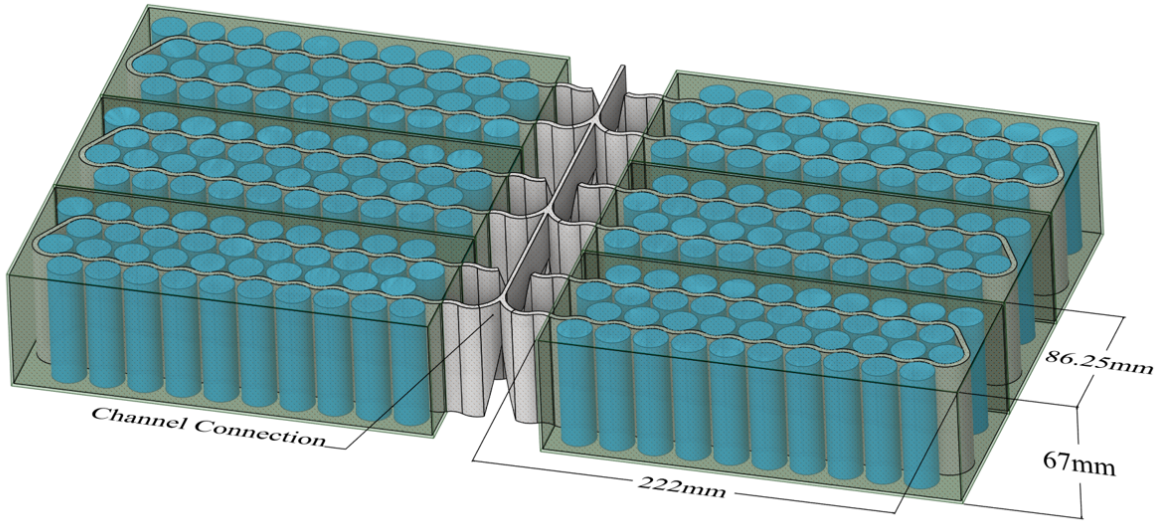

Figure 5.1: Geometry of 6 battery modules

The fireproof material of aerogel is placed between each two battery packs, which reserve space for the flow channel to pass inside. On the one hand, this makes the structure between the battery packs more compact and saves space in the wings. On the other hand, the good thermal insulation ability of the fireproof material itself reduces the unnecessary heat transfer of the flow channel to other components.

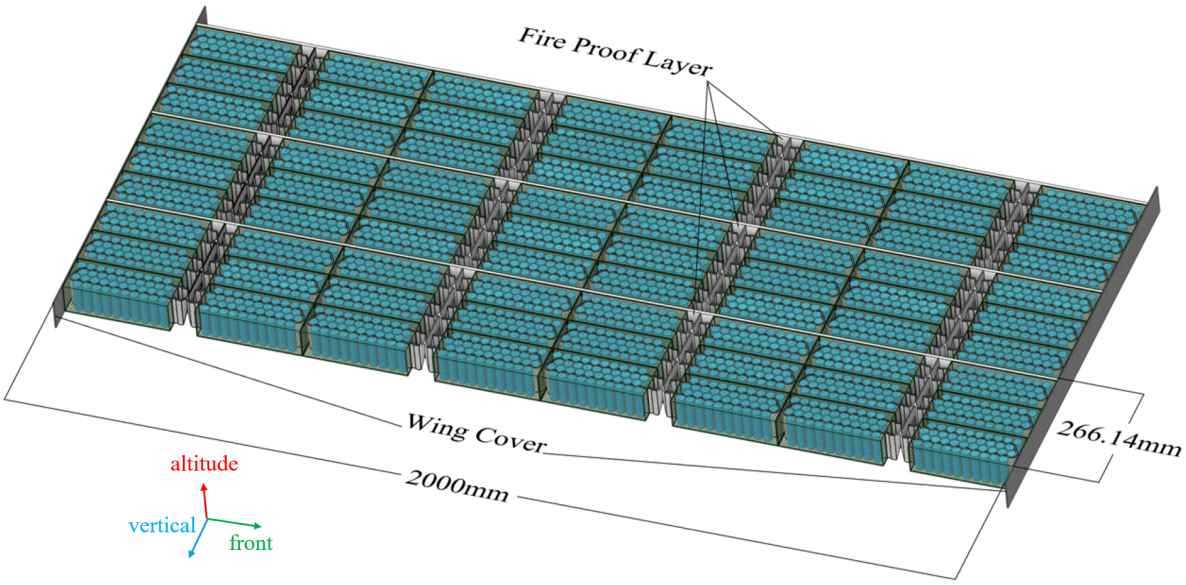

Figure 5.2: Geometry of 3 battery packs

After the shape of the battery pack has been designed, it needs to be verified that it can fit inside the wing.

In quantity, based on the results in Chapter.**??**, the minimum number of required cell is 67137. With 40 cells per module, the minimum number of modules required is 1679 (rounded up). Similarly, there are 24 modules in each battery pack, and the minimum number of battery packs required is 70 (rounded up). Considering the balance of the weight in the aircraft, 35 battery packs are placed on each wing.

In size, based on Chapter.4, the external size of the module is determined to be 222mm × 88mm × 67mm (front × vertical × altitude). The modules are arranged in 8 rows, 3 columns and 1 layer in the battery pack, so the minimum external size of the battery pack is 1.776m ×0.258m ×0.067m. Considering to reserve space for the connection structure between modules and the stationary structure of the module, the external dimension of the battery pack is designed as 2m× 0.26m ×0.07m. Since 35 packs are arranged in vertical direction in each wing as shown in Fig.5.3, minimum total dimension of 35 battery packs is 2m× 9.1m× 0.07m.

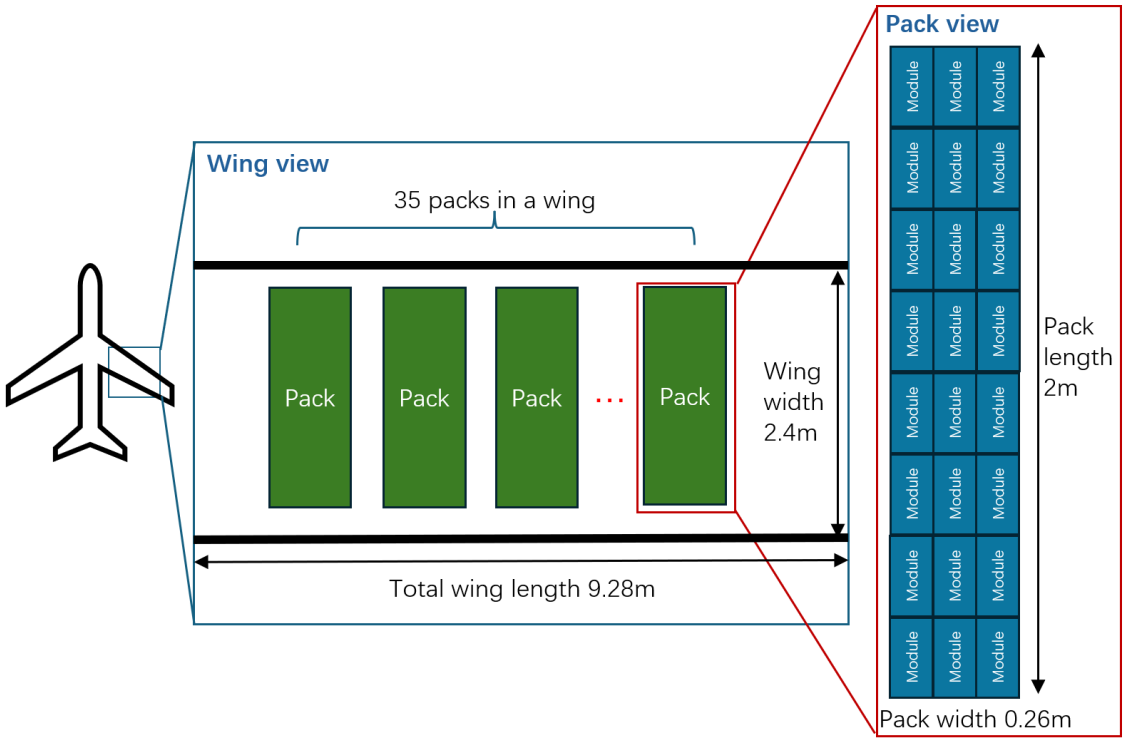

Figure 5.3: Layout of the battery pack on the wing

The PC-12 conventional aircraft has 16.28m wing span and 25.81m^2 wing area[56]. Minus the fuselage width and the tip width, the single wing length is 6.4m. The wing shape is assumed to conform to a rectangular straight wing. Therefore, the wing dimension of the conventional aircraft is 2.02m× 6.4m (front× vertical).

In the case of satisfying the wing unit area load calculated in Chapter.**??**, the total wing area of the AEA in this design increases to at least 49.80m^2. In the design, the wing remains the same shape and the size is enlarged in equal proportion, thus:

$$\alpha^2 A_{\mathrm{w,ref}} = A_{\mathbf{w}} \tag{5.1}$$

$$\alpha D_{\mathrm{ws,ref}} = D_{\mathbf{ws}} \tag{5.2}$$

$$\alpha D_{\mathrm{ww,ref}} = D_{\mathbf{ww}} \tag{5.3}$$

where α is the proportionality coefficient, $A_{\mathrm{w,ref}}$ $D_{\mathrm{ws,ref}}$ $D_{\mathrm{ww,ref}}$ are respectively the wing area, wing span in vertical direction and wing width in front direction of the conventional reference aircraft, and A_{w} D_{ws} D_{ww} are respectively the wing area, wing span in vertical direction and wing width in front direction of the AEA.

Set α as 1.45, the wing dimension of the AEA is 2.92m× 9.28m (front× vertical), which would leave enough room for the battery pack and enough spare space for other components. The wing area of the AEA is 54.20m^2, which is enough for take-off. The distribution of battery pack in the wing is shown in Fig,5.4.

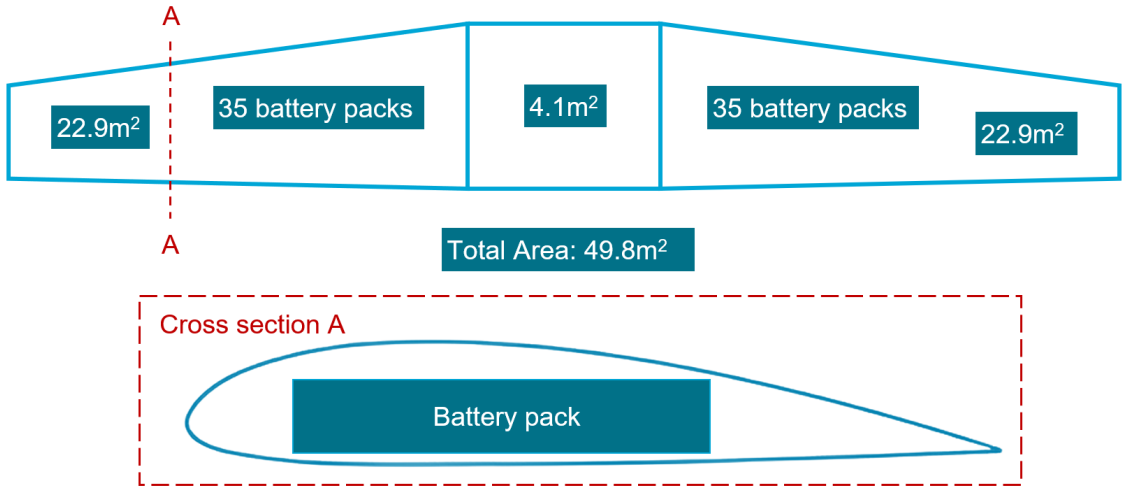

Figure 5.4: Distribution of the battery pack in the wing

5.2. CFD Simulation

The simulation of battery pack level aims to explore whether the thermal insulation design of the battery modules is adequate when the temperature of the battery pack is affected by the heat transfer between each other, and whether the differences in thermal performance of battery modules within the battery pack are acceptable. Considering that the geometric structure, the thermal resistance and heating structure of each battery pack are consistent, and the thickness of the fire proof layer between the battery packs is considered to be thick enough, the thermal characteristics of each battery pack are regarded as the same in this thesis. Thus, the simulation is carried out for a single battery pack.

5.2.1. Initial and Boundary Conditions

To simplify the calculation, the following assumptions are made in this thesis:

The battery pack is thermally conductive only on the surfaces that are in contact with the metal of the wing, and because of the excellent thermal conductivity of these materials, the temperature of these surfaces is always in line with the temperature of the outside atmosphere. The rest of the surface is in contact with the fireproof material and is regarded as an adiabatic surface.

The temperature value profile of the internal components of the battery module (battery cell and flow channel) over time in Chapter. 4 is used as the battery module temperature in the battery pack model. This assumption is based on the low heat transfer between the cell and the outside world, which is not sufficient to significantly affect the cell temperature. Therefore, the complex simulation of all battery cells in the battery pack is avoided.

5.2.2. Result and Conclusion

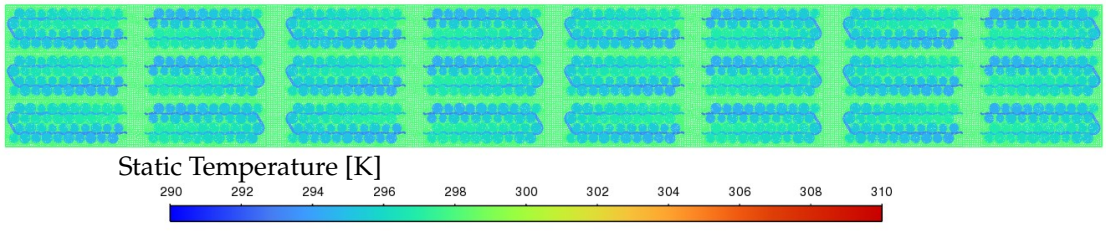

Figure 5.5: Temperature contour of battery pack at at 1553s

The result of simulation at at 1553s is shown in Fig.5.5. It can be seen that the temperature distribution of each module is almost exactly the same. This is because all the gaps except the cell, the flow channel and the package are filled with air, and the spatial structure constraints of the battery pack make this air almost stationary. Still air has an extremely low thermal conductivity and therefore acts as a good insulation material. as a result, the thermal insulation capability of the battery module is verified.

6

Discussion and Conclusion

This chapter aims to summarize the work carried out in the thesis. The content includes a summary of the degree of completion of the goals proposed in Chapter.1, a discussion of the limitations of this thesis and an exposition of future work that is helpful to this design.

6.1. Conclusion

The aim of this thesis is to design a battery pack for the application scenario of a regional AEA. The current challenges of battery technology for AEA are specific energy, temperature uniformity and stability of the battery pack. Therefore, it is necessary to provide the battery pack design with the highest specific energy under the premise that the BTMS meets the uniform and stable cell temperature. Firstly, this thesis analyzed the demand of flight, and then sized the battery pack to fulfill the demand. Then, based on the size, the model building process in this thesis is analyzed, modeled and simulated in turn from small to large, from the cell, the module to the pack level.

The main research question is answered as following:

1) How to analyse the AEA flight energy demand and how will this decide the size of battery pack?

First the flight power demand of AEA is calculated using flight mechanics, in Chapter.2. Based on the Pilatus PC-12 traditional aircraft modification, the corresponding AEA specifications are calculated under reasonable assumptions. The flight is divided into four main phases: take-off, climb, cruise and descent. The energy and power of these phases are calculated separately based on the balance of forces on aircraft. The result shows that take-off, climb, cruise and descent phases require power of 1888.75kW, 1040.06kW, 408.563kW and 34.2109kW. Thesis phases have a total energy demand of 807.4359kWh, which should be provided by the battery pack. In this thesis, Samsung INR18650-35E NMC battery cell is selected due to its high energy density, well-established technology, and strong battery supply chain which is ready to use. Because of the round series and parallel number of the cells in the battery pack, the energy of the designed battery pack will not be just equal to the flight energy demand, and the actual design energy of the battery pack is 809.672kWh.

2) How to simulate the battery cell electrical and thermal behavior in the discharge?

In Chapter.3, the second-order ECM model is used to describe the discharge characteristics of the cell. Experiments were performed to obtain equations for the various parameters of the ECM model. The fitting accuracy of the formula is expressed as The mean absolute percentage error, For R_0, R_s, C_s, R_l and C_l precision are respectively 3%, 21%, 10%, 30% and 18%.. After the investigation, analysis and simulation of the thermal behavior of the cell, the model is simplified to reduce the calculation while retaining the thermodynamic characteristics of the cell. The cell heating model is simplified to be

uniform. Based on the available finite element analysis results, the cell heat transfer model is simplified to have anisotropic thermal conductivity. The 3D simulation of the above model packed in the module shows that the axial temperature difference of the cell is not obvious, so the model is simplified to 2D and the axial heat transfer is neglected.

3) How to design the BTMS of the battery module?

In Chapter.4, in view of the electric safety of battery pack, sufficient cooling effect, low difficulty of control and maintenance, indirect liquid cooling is selected by this design as the thermal management method. The thermal performance of multiple cells in the module under BTMS is simulated, and the thermal performance of the cells under different conditions is shown in Fig.4.5,4.8 and 4.12 to 4.14. Based on these results, the flow rate control and geometric parameters of modules are optimized by focusing on the stability and uniformity of the cell temperature and the energy density of the battery pack. Finally, the battery module with 2mm cell spacing, 0.4mm flow channel wall thickness, 1mm packaging thickness, and constant flow rate control had the best temperature characteristics and lowest energy consumption.

4) Is the design of the battery pack appropriate?
In Chapter.5, the geometric dimension of the battery pack is designed and verified by the dimension of the space for battery storage. Then, in order to observe the effect of BTMS at the battery pack level, simulation were performed. The results show that the thermal insulation design of the battery module is sufficient to make the thermal performance difference between battery modules caused by external heat transfer within an acceptable range.

6.2. Discussion

Many of the methods used in this study have uncertainties and limitations, which are listed as follow:

6.2.1. All Electric Aircraft

The electric aircraft is modified from the reference conventional aircraft PC-12 design. Although the design of relevant parameters of the reference aircraft is close to maturity and the product has been put into use, it is difficult to predict the changes occurring in the process of electrification. In this thesis, the modification of the wing is regarded as an equal scale enlargement to isolate the influence of modifications of other aircraft components on it. In practice, the design of the all the components of the aircraft will affect each other. For example, airfoils will be redesigned to cope with new aircraft loads and flight cycles, and this will affect the available space for battery packs in the wings.

6.2.2. Model

In this thesis, through analysis and simulation results verification, it is believed that the cell model can still reflect its thermodynamic characteristics after simplifying to 2D. However, this simplification needs to be supported by actual experimental data. A measurement of the temperature spatial distribution inside the battery cell when it is generating heat is needed to determine the reasonability of the 2D simplification.

The refrigerant control method in this thesis uses a combination of constant temperature and variational flow rate. However, if only considering the technical difficulty, the constant flow rate output with variational temperature is easier for the refrigeration cycle that supplies the refrigerant to the BTMS, because in most refrigeration cycles the flow rate is usually fixed and the temperature control is achieved by adjusting the compressor power. The control system and technology in this way are more mature. If the only consideration is more flexible thermal management, the refrigerant control with variable temperature and flow rate can be used to adjust the cooling capacity most accurately.

6.2.3. Optimization

The parameters selected for the optimization in this thesis are limited. For example, the effect of changes in the number of cells in a single module is ignored in this thesis. If the number of cells in the module and the flow velocity of the fluid in the flow channel are increased simultaneously, the energy density of the battery pack may be further increased while ensuring temperature uniformity. Moreover, only a few groups of simulations are carried out for each parameter when optimizing in this thesis. Increasing the density of test points for a given parameter may lead to a better approximation of the optimal parameter value. In addition, the influence of each parameter on the module is tested separately, but the effect of these parameters on the module may not be completely independent. The combined effect of each parameter requires multi-objective optimization method.

In this thesis, the parameters in the governing equations of the refrigerant flow rate are determined by simulation attempts, and no optimization analysis is carried out. In batter optimization, the characteristics of heat generation during flight should be grasped, and the step and climb process should be simulated separately to observe the performance of control.

6.3. Future Work

Regional AEA is an immature research area, and the technologies related to its design and production are still developing rapidly. This study provides a preliminary design of battery packs for AEA, which can be used as a basis for future research work:

- Design and simulate for battery packs of different chemical types and different shapes of the cell to select the best type more reasonably.
- Combine the design of the BTMS with the other part of the Battery Management System (BMS) to design a complete battery system.
- Test Battery packs for electric aircraft experimentally. According to the results of the corresponding simulation, the experiment can be designed, and the multi-objective optimization of the battery pack can be carried out on the basis of the experimental results, so as to obtain a design scheme closer to the actual application. At the same time, the selected optimization objective should be more comprehensive, including more complex fluid control and more variety of flow channels, etc.
- Tune the refrigerant flow rate PD control. The step and climb processes of battery heat generation in flight can be separated and used as input signals to test the control system for optimization.

References

[1] European Commission. *Reducing emissions from aviation*. URL: https://climate.ec.europa.eu/eu-action/transport/reducing-emissions-aviation_en#events.

[2] M Darecki et al. *European Commission, Directorate-General for Mobility and Transport, Directorate-General for Research and Innovation, Flightpath 2050: Europe's Vision for Aviation: Maintaining Global Leadership and Serving Society's Needs*. 2011.

[3] Francesco Salucci et al. "A noise estimation procedure for electric and Hybrid-Electric aircraft". In: *AIAA Scitech 2021 Forum* (Jan. 2021). DOI: 10.2514/6.2021-0258. URL: https://doi.org/10.2514/6.2021-0258.

[4] Andreas W. Schäfer et al. "Technological, economic and environmental prospects of all-electric aircraft". In: *Nature energy* 4.2 (Dec. 2018), pp. 160–166. DOI: 10.1038/s41560-018-0294-x. URL: https://doi.org/10.1038/s41560-018-0294-x.

[5] Dennis L. Huff, Brenda S. Henderson, and Edmane Envia. "Motor Noise for Electric Powered Aircraft". In: *22nd AIAA/CEAS Aeroacoustics Conference* (May 2016). DOI: 10.2514/6.2016-2882. URL: https://doi.org/10.2514/6.2016-2882.

[6] Robert Thomson. *Electric propulsion is finally on the map*. May 2018. URL: https://www.rolandberger.com/en/Insights/Publications/Electric-propulsion-is-finally-on-the-map.html.

[7] Diane Selkirk. *Is this the start of an aviation revolution?* Feb. 2022. URL: https://www.bbc.com/future/article/20200211-the-electric-plane-leading-a-revolution.

[8] J.A. Rosero et al. "Moving towards a more electric aircraft". In: *IEEE Aerospace and Electronic Systems Magazine* 22.3 (Mar. 2007), pp. 3–9. DOI: 10.1109/maes.2007.340500. URL: https://doi.org/10.1109/maes.2007.340500.

[9] Jack D. Mattingly. *Elements of propulsion: gas turbines and rockets*. Vol. 29. American Institute of Aeronautics and Astronautics, Jan. 2006. DOI: 10.2514/4.861789. URL: https://doi.org/10.2514/4.861789.

[10] Yawen Liang et al. "Charging demand prediction: small All-Electric aircraft and electric vertical takeoff and landing aircraft". In: *IEEE Transactions on Transportation Electrification* (Jan. 2024), p. 1. DOI: 10.1109/tte.2024.3427841. URL: https://doi.org/10.1109/tte.2024.3427841.

[11] Michael D Patterson, Brian J German, and Mark D Moore. "Performance analysis and design of on-demand electric aircraft concepts". In: *12th AIAA Aviation Technology, Integration, and Operations (ATIO) Conference and 14th AIAA/ISSMO Multidisciplinary Analysis and Optimization Conference*. 2012.

[12] Taewoo Nam. "A generalized sizing method for revolutionary concepts under probabilistic design constraints". PhD thesis. Citeseer, 2007.

[13] Jeff Chin et al. "Battery Cell-to-Pack scaling trends for electric aircraft". In: *AIAA Propulsion and Energy 2021 Forum* (July 2021). DOI: 10.2514/6.2021-3316. URL: https://doi.org/10.2514/6.2021-3316.

[14] Zachary Heit and Susan Liscouet-Hanke. "Estimation of battery pack layout and dimensions for the conceptual design of Hybrid-Electric aircraft". In: *AIAA SCITECH 2023 Forum* (Jan. 2023). DOI: 10.2514/6.2023-1362. URL: https://doi.org/10.2514/6.2023-1362.

[15] Guodong Xia, Lei Cao, and Guanglong Bi. "A review on battery thermal management in electric vehicle application". In: *Journal of power sources* 367 (2017), pp. 90–105.

[16] Daeyeun Kim et al. "A numerical study of the suitability of Phase-Change materials for battery thermal management in flight applications". In: *World Electric Vehicle Journal* 14.1 (Jan. 2023), p. 15. DOI: 10.3390/wevj14010015. URL: https://doi.org/10.3390/wevj14010015.

[17] Hagen Kellermann et al. "Design of a battery cooling system for hybrid electric aircraft". In: *Journal of Propulsion and Power* 38.5 (Sept. 2022), pp. 736–751. DOI: 10.2514/1.b38695. URL: https://doi.org/10.2514/1.b38695.

[18] Thomas Kuijpers, Jorn van Kampen, and Theo Hofman. "System-level thermal and electrical modeling of battery systems for electric aircraft design". In: *arXiv preprint arXiv:2408.16494* (2024).

[19] Ravi Annapragada et al. "Hybrid Electric Aircraft Battery Heat Acquisition System". In: *IEEE* (July 2018). DOI: 10.2514/6.2018-4992. URL: https://doi.org/10.2514/6.2018-4992.

[20] William L. Fredericks et al. "Performance metrics required of Next-Generation batteries to electrify vertical takeoff and landing (VTOL) aircraft". In: *ACS Energy Letters* 3.12 (Nov. 2018), pp. 2989–2994. DOI: 10.1021/acsenergylett.8b02195. URL: https://doi.org/10.1021/acsenergylett.8b02195.

[21] Shashank Sripad, Alexander Bills, and Venkatasubramanian Viswanathan. "A review of safety considerations for batteries in aircraft with electric propulsion". In: *MRS bulletin* 46.5 (May 2021), pp. 435–442. DOI: 10.1557/s43577-021-00097-1. URL: https://link-springer-com.tudelft.idm.oclc.org/article/10.1557/s43577-021-00097-1#citeas.

[22] Alexander Barke et al. "Life cycle sustainability assessment of potential battery systems for electric aircraft". In: *Procedia CIRP* 98 (Jan. 2021), pp. 660–665. DOI: 10.1016/j.procir.2021.01.171. URL: https://doi.org/10.1016/j.procir.2021.01.171.

[23] Reynard De Vries, Malcom T. Brown, and Roelof Vos. "A preliminary sizing method for Hybrid-Electric aircraft including Aero-Propulsive interaction effects". In: *2018 Aviation Technology, Integration, and Operations Conference* (June 2018). DOI: 10.2514/6.2018-4228. URL: https://doi.org/10.2514/6.2018-4228.

[24] Editor Engineeringtoolbox. *U.S. Standard Atmosphere vs. Altitude*. Apr. 2024. URL: https://www.engineeringtoolbox.com/standard-atmosphere-d_604.html.

[25] Mingtai Chen. "Static thrust measurement for propeller-driven light aircraft". In: *2012 International Conference on Computer Application and System Modeling*. Atlantis Press. 2012, pp. 650–652.

[26] Carlo E.D. Riboldi. "Energy-optimal off-design power management for hybrid-electric aircraft". In: *Aerospace Science and Technology* 95 (Dec. 2019), p. 105507. DOI: 10.1016/j.ast.2019.105507. URL: https://doi.org/10.1016/j.ast.2019.105507.

[27] P. Sforza. *Chapter 8- refined weight and balance estimate*. Jan. 2014, pp. 301–347. DOI: 10.1016/b978-0-12-419953-8.00013-9. URL: https://doi.org/10.1016/b978-0-12-419953-8.00013-9.

[28] *Earth Atmosphere Model - Metric Units*. May 2021. URL: https://www.grc.nasa.gov/WWW/K-12/airplane/atmosmet.html.

[29] Burak Tarhan, Ozge Yetik, and Tahir Hikmet Karakoc. "Hybrid battery management system design for electric aircraft". In: *Energy* 234 (Nov. 2021), p. 121227. DOI: 10.1016/j.energy.2021.121227. URL: https://doi.org/10.1016/j.energy.2021.121227.

[30] Mohd Tariq et al. "Aircraft batteries: current trend towards more electric aircraft". In: *IET electrical systems in transportation* 7.2 (June 2017), pp. 93–103. DOI: 10.1049/iet-est.2016.0019. URL: https://doi.org/10.1049/iet-est.2016.0019.

[31] George E. Blomgren. "The development and future of lithium ion batteries". In: *Journal of the Electrochemical Society* 164.1 (Dec. 2016), A5019–A5025. DOI: 10.1149/2.0251701jes. URL: https://doi.org/10.1149/2.0251701jes.

[32] Ltd. Samsung SDI Co. *SPECIFICATION OF PRODUCT for Lithium-ion rechargeable cell*. July 2015. URL: https://www.orbtronic.com/content/samsung-35e-datasheet-inr18650-35e.pdf.

[33] Eric Maiser. "Battery packaging - Technology review". In: *AIP conference proceedings* (Jan. 2014). DOI: 10.1063/1.4878489. URL: https://doi.org/10.1063/1.4878489.

[34] Robert Schröder, Muhammed Aydemir, and Günther Seliger. "Comparatively Assessing different Shapes of Lithium-ion Battery Cells". In: *Procedia manufacturing* 8 (Jan. 2017), pp. 104–111. DOI: 10.1016/j.promfg.2017.02.013. URL: https://doi.org/10.1016/j.promfg.2017.02.013.

[35] Venkatasubramanian Viswanathan et al. "The challenges and opportunities of battery-powered flight". In: *Nature* 601.7894 (Jan. 2022), pp. 519–525. DOI: 10.1038/s41586-021-04139-1. URL: https://www-nature-com.tudelft.idm.oclc.org/articles/s41586-021-04139-1.

[36] Hendrik Schefer et al. "Discussion on electric power supply systems for all electric aircraft". In: *IEEE Access* 8 (Jan. 2020), pp. 84188–84216. DOI: 10.1109/access.2020.2991804. URL: https://doi.org/10.1109/access.2020.2991804.

[37] Monowar Hossain et al. "A Parameter Extraction Method for the Thevenin Equivalent Circuit Model of Li-ion Batteries". In: *In Proceedings of the 2019 IEEE Industry Applications Society Annual Meeting* (Sept. 2019). DOI: 10.1109/ias.2019.8912326. URL: https://doi.org/10.1109/ias.2019.8912326.

[38] Kaiyuan Li et al. "A practical Lithium-Ion battery model for state of energy and voltage responses prediction incorporating temperature and ageing effects". In: *IEEE transactions on industrial electronics* 65.8 (Aug. 2018), pp. 6696–6708. DOI: 10.1109/tie.2017.2779411. URL: https://doi.org/10.1109/tie.2017.2779411.

[39] None Long Lam, Pavol Bauer, and Erik Kelder. "A practical circuit-based model for Li-ion battery cells in electric vehicle applications". In: *IEEE* (Oct. 2011). DOI: 10.1109/intlec.2011.6099803. URL: https://doi.org/10.1109/intlec.2011.6099803.

[40] Lisa Kathrin Willenberg, Ulrich Simon, and Dirk Uwe Sauer. "Volumenausdehnung und ihre Auswirkungen auf die Alterung einer zylindrischen Lithium-Ionen-Batterie". In: *ISEA* (Jan. 2020). DOI: 10.18154/rwth-2021-01906. URL: http://publications.rwth-aachen.de/record/813702.

[41] Hartmut Popp et al. "Ante-mortem analysis, electrical, thermal, and ageing testing of state-of-the-art cylindrical lithium-ion cells". In: *Elektrotechnik und Informationstechnik/Elektrotechnik und Informationstechnik* 137.4-5 (June 2020), pp. 169–176. DOI: 10.1007/s00502-020-00814-9. URL: https://doi.org/10.1007/s00502-020-00814-9.

[42] D. Bernardi, E. Pawlikowski, and J. Newman. "A general energy balance for battery systems". In: *Journal of the Electrochemical Society* 132.1 (Jan. 1985), pp. 5–12. DOI: 10.1149/1.2113792. URL: https://doi.org/10.1149/1.2113792.

[43] Ahmad A. Pesaran. "Battery thermal models for hybrid vehicle simulations". In: *Journal of power sources* 110.2 (Aug. 2002), pp. 377–382. DOI: 10.1016/s0378-7753(02)00200-8. URL: https://doi.org/10.1016/s0378-7753(02)00200-8.

[44] Bruno Scrosati, Jurgen Garche, and Werner Tillmetz. *Advances in battery technologies for electric vehicles*. Woodhead Publishing, May 2015.

[45] S.J. Wright, D.W. Dixon-Hardy, and P.J. Heggs. "Aircraft air conditioning heat exchangers and atmospheric fouling". In: *Thermal science and engineering progress* 7 (Sept. 2018), pp. 184–202. DOI: 10.1016/j.tsep.2018.06.007. URL: https://doi.org/10.1016/j.tsep.2018.06.007.

[46] A Pesaran and GH Kim. *Battery thermal management system design modeling*. Tech. rep. National Renewable Energy Lab.(NREL), Golden, CO (United States), 2006.

[47] Xiaojun Tan et al. "Numerical investigation of the direct liquid cooling of a fast-charging lithium-ion battery pack in hydrofluoroether". In: *Applied thermal engineering* 196 (Sept. 2021), p. 117279. DOI: 10.1016/j.applthermaleng.2021.117279. URL: https://doi.org/10.1016/j.applthermaleng.2021.117279.

[48] Jiwen Cen and Fangming Jiang. "Li-ion power battery temperature control by a battery thermal management and vehicle cabin air conditioning integrated system". In: *Energy Sustainable Development/Energy for sustainable development* 57 (Aug. 2020), pp. 141–148. DOI: 10.1016/j.esd.2020.06.004. URL: https://doi.org/10.1016/j.esd.2020.06.004.

[49] Gaoliang Liao et al. "Thermal performance of lithium-ion battery thermal management system based on nanofluid". In: *Applied Thermal Engineering* 216 (Nov. 2022), p. 118997. DOI: 10.1016/j.applthermaleng.2022.118997. URL: https://doi.org/10.1016/j.applthermaleng.2022.118997.

[50] Jonathan Harrison et al. “Using multi-physics system simulation to predict battery pack thermal performance and risk of thermal runaway during EVTOL aircraft operations”. In: *AIAA Propulsion and Energy 2019 Forum* (Aug. 2019). DOI: 10.2514/6.2019-4406. URL: https://doi.org/10.2514/6.2019-4406.

[51] Peter Thomas Tennessen et al. *Extruded and Ribbed Thermal Interface for use with a Battery Cooling System - Google Patents*. June 2007. URL: https://patents.google.com/patent/US20110212356A1/en?oq=20110212356#patentCitations.

[52] Deepak Gautam et al. “Performance comparison of thermal interface materials for power electronics applications”. In: *IEEE* (Mar. 2014). DOI: 10.1109/apec.2014.6803814. URL: https://doi.org/10.1109/apec.2014.6803814.

[53] Jin Tang et al. “Suppressing thermal runaway propagation of nickel-rich Lithium-ion battery modules using silica aerogel sheets”. In: *Process safety and environmental protection/Transactions of the Institution of Chemical Engineers. Part B, Process safety and environmental protection/Chemical engineering research and design/Chemical engineering research & design* 179 (Nov. 2023), pp. 199–207. DOI: 10.1016/j.psep.2023.08.100. URL: https://doi.org/10.1016/j.psep.2023.08.100.

[54] Quanyi Liu et al. “Influence of Aerogel Felt with Different Thickness on Thermal Runaway Propagation of 18650 Lithium-ion Battery”. In: *Electrochemistry* 90.8 (Aug. 2022), p. 087003. DOI: 10.5796/electrochemistry.22-00048. URL: https://doi.org/10.5796/electrochemistry.22-00048.

[55] Todd M Bandhauer, Srinivas Garimella, and Thomas F Fuller. “A critical review of thermal issues in lithium-ion batteries”. In: *Journal of the electrochemical society* 158.3 (2011), R1.

[56] PILATUS. *PC-12 NG OVERVIEW*. https://web.archive.org/web/20161009041729/http://www.pilatus-aircraft.com/00-def/main/scripts/ckfinder/userfiles/files/Downloads/Brochures/Pilatus-Aircraft-Ltd-PC-12NG-JustTheFacts.pdf. Accessed: 2024-9-12.

A

Thevenin Equivalent Circuit Model Parameter Identification Coefficient

V_{OC}	
a_{1OCV}	-0.8158
a_{2OCV}	0.4339
a_{3OCV}	3.316
a_{4OCV}	0.008692

R_0	
a_{1R0}	1.12774685e+07
a_{2R0}	-2.36775439e+05
a_{3R0}	6.95730070e+03
a_{4R0}	-8.57920276e+01
a_{5R0}	3.79691090e-01
b_{1R0}	7.14427587e-09
b_{2R0}	9.67955610e+02
b_{3R0}	-2.69097188e+02
c_{1R0}	1.36546647e-03
c_{2R0}	2.43985680e+00
c_{3R0}	3.54177981e-02

R_s	
a_{1Rs}	1.96803076e+06
a_{2Rs}	-2.58332869e+05
a_{3Rs}	1.53159190e+04
a_{4Rs}	-4.43425086e+02
a_{5Rs}	6.65600564e+00
a_{6Rs}	-4.96741336e-02
a_{7Rs}	1.45632742e-04
b_{1Rs}	-2.48574374e+03
b_{2Rs}	6.54688868e+02
b_{3Rs}	-1.23415311e+02
b_{4Rs}	8.44494379e+00
b_{5Rs}	-2.37800677e-01
b_{6Rs}	2.34962550e-03
c_{1Rs}	-2.85171770e-11
c_{2Rs}	3.57970697e-11
c_{3Rs}	-3.37765236e-11
c_{4Rs}	1.63956047e-11
c_{5Rs}	-3.26665166e-12

C_s	
a_{1Cs}	2.03862268e+09
a_{2Cs}	1.11506082e+09
a_{3Cs}	-3.21726508e+07
a_{4Cs}	3.08620146e+05
a_{5Cs}	1.25648168e+03
a_{6Cs}	-3.94023327e+01
a_{7Cs}	1.76420523e-01
b_{1Cs}	3.32064926e+03
b_{2Cs}	-4.53277892e+02
b_{3Cs}	1.09336855e+02
b_{4Cs}	-7.21817644e+00
b_{5Cs}	1.96161941e-01
b_{6Cs}	-1.88247465e-03
c_{1Cs}	-7.78869166e-10
c_{2Cs}	1.21168221e-03
c_{3Cs}	7.96829568e-10

R_l	
a_{1Rl}	2.05815024e+06
a_{2Rl}	-1.56156844e+05
a_{3Rl}	4.97139500e+03
a_{4Rl}	-6.35780843e+01
a_{5Rl}	2.89204394e-01
b_{1Rl}	1.71831343e-07
b_{2Rl}	5.04501506e-02
b_{3Rl}	-7.80182300e-09
c_{1Rl}	9.70216081e-01
c_{2Rl}	-1.76219586e+00
c_{3Rl}	1.49528344e+00
c_{4Rl}	-5.21393126e-01
d_{1Rl}	1.26452053e-02

C_l	
a_{1Cl}	2.74350258e-01
a_{2Cl}	-1.99345918e-02
a_{3Cl}	2.64036001e-03
a_{4Cl}	-8.20580141e-05
a_{5Cl}	9.75157146e-07
a_{6Cl}	-3.98718332e-09
b_{1Cl}	4.84342144e+06
b_{2Cl}	1.43475014e+05
b_{3Cl}	2.98133711e+03
b_{4Cl}	8.47321832e-01
b_{5Cl}	-5.08963215e+00
b_{6Cl}	1.07937317e-01
c_{1Cl}	5.41920941e-04
c_{2Cl}	4.08544931e-04
c_{3Cl}	-1.45601744e-04
c_{4Cl}	1.38701541e-04
c_{5Cl}	-4.36981999e-05

Table.A ECM Parameter Identification Coefficient